

Suppression of Antiferromagnetic Order by Strain in Honeycomb Cobaltate: Implication for Quantum Spin Liquid

Gye-Hyeon Kim,^{1*} Miju Park,^{1*} Uksam Choi,¹ Baekjune Kang,¹ Uihyeon Seo,¹ GwangCheol Ji,² Seunghyeon Noh,³ Deok-Yong Cho,⁴ Jung-Woo Yoo,³ Jong Mok Ok,² and Changhee Sohn^{1†}

¹Department of Physics, Ulsan National Institute of Science and Technology, Ulsan, 44919, Republic of Korea

²Department of Physics, Pusan National University, Pusan, 46241, Republic of Korea

³Department of Materials Science and Engineering, Ulsan National Institute of Science and Technology, Ulsan, 44919, Republic of Korea

⁴Department of Physics, Jeonbuk National University, Jeonju, 54896, Republic of Korea

Abstract

Recently, layered honeycomb cobaltates have been predicted as a new promising system for realizing the Kitaev quantum spin liquid, a many-body quantum entangled ground state characterized by fractional excitations. However, these cobaltates, similar to other candidate materials, exhibit classical antiferromagnetic ordering at low temperatures, which impedes the formation of the expected quantum state. Here, we demonstrate that the control of the trigonal crystal field of Co ions is crucial to suppress classical antiferromagnetic ordering and to locate its ground state in closer vicinity to quantum spin liquid in layered honeycomb cobaltates. By utilizing heterostructure engineering on $\text{Cu}_3\text{Co}_2\text{SbO}_6$ thin films, we adjust the trigonal distortion of CoO_6 octahedra and the associated trigonal crystal field. The original Néel temperature of 16 K in bulk $\text{Cu}_3\text{Co}_2\text{SbO}_6$ decreases (increases) to 7.8 K (22.7 K) in strained $\text{Cu}_3\text{Co}_2\text{SbO}_6$ films by decreasing (increasing) the magnitude of the trigonal crystal fields. Our experimental finding substantiates the potential of layered honeycomb cobaltate heterostructures and strain engineering to accomplish the extremely elusive quantum phase of matter.

I. INTRODUCTION

The small amount of broken local symmetry has been blamed for making a whole many-body quantum entangled state collapse into a (quasi)classical product state. Ever since P. W. Anderson's idea of resonating valence bond [1,2], searching for many-body quantum entangled ground states and low-energy excitation in the matter has remained an important, but highly elusive task in condensed matter physics [3-5]. An outstanding example is the Kitaev quantum spin liquid (QSL), in which bond-dependent Ising interactions of spins on a two-dimensional honeycomb lattice induce macroscopic quantum entanglement and fractional excitations [6]. While intensive studies have found signatures of fractionalization in candidate materials such as Na_2IrO_3 [7-11] and $\alpha\text{-RuCl}_3$ [12-18], all of them have shown classical long-range antiferromagnetic orderings at sufficiently low temperatures (T). The convincing hypotheses about the collapse of the predicted quantum state in low T have pointed out broken local symmetry as a culprit [10,18]. For example, finite trigonal distortions act as one of the main effects in generating non-Kitaev spin interactions in various candidate materials [18-20], deviating from the original concept of realizing Kitaev QSL through edge-shared cubic octahedra as shown in Fig. 1(a) [21]. Therefore, experimental verification of strong correlations between local distortions and stability of classical ground states would mark a significant milestone in realizing these notoriously elusive quantum phases of matter.

In this context, $\text{Cu}_3\text{Co}_2\text{SbO}_6$, a layered honeycomb cobaltate, can be an exemplary model system for probing the hypothesized relationship between local trigonal distortion and magnetic ground state. Recent theoretical [19,22-24] and experimental [25-29] studies suggested layered honeycomb cobaltate can be in close vicinity of Kitaev QSL as their orbital structures can be described as spin-orbit entangled $J_{\text{eff}} = 1/2$ states [23]. However, due to the relatively small spin-orbit coupling strength of Co ions, the presence of compressive trigonal distortion is expected to break $J_{\text{eff}} = 1/2$ orbital pictures rather easily, favoring the stabilization of a single a_{1g} and doubly degenerate e_g orbitals [Fig. 1(a)] [30]. Therefore, previous theoretical studies suggested that the Kitaev QSL state could be realized only with a small trigonal crystal field (Δ_{trig}) in the layered honeycomb cobaltates [23]. As shown in Fig. 1(b), $\text{Cu}_3\text{Co}_2\text{SbO}_6$ has distorted local octahedra and displays classical antiferromagnetic ordering near 16 K [31] consistent with the aforementioned theoretical hypotheses. Notably, unlike other Kitaev material candidates, this compound has been successfully synthesized in thin film [32], facilitating the application of lattice engineering, which enables manipulation of local

distortion of CoO_6 octahedra [33-35].

Here, we present experimental evidence that the control of the local Δ_{trig} induces a wide modulation in the Néel temperature (T_N) of $\text{Cu}_3\text{Co}_2\text{SbO}_6$. By utilizing $\text{Cu}_3\text{Co}_2\text{SbO}_6$ (001) film grown on ZnO (0001) substrate [32], we successfully manipulated the trigonal distortion of the CoO_6 octahedra and Δ_{trig} of Co ions [Fig. 1(c)]. We observed that the ultrathin $\text{Cu}_3\text{Co}_2\text{SbO}_6$ film got strained on the ZnO substrate, notwithstanding the large lattice mismatch (+ 4.3 %). This strain allowed us to stretch the octahedra in the in-plane direction, resulting in an increased compressive trigonal distortion. Due to the absence of a suitable substrate for out-of-plane stretching in the octahedra, we conducted helium implantation on the bulk-like 20-unit cell (u.c.) $\text{Cu}_3\text{Co}_2\text{SbO}_6$ films. This is a well-known methodology for out-of-plane expansion of CoO_6 octahedra thereby mitigating the compressive trigonal distortion [35]. X-ray absorption spectroscopy (XAS) reveals a clear increase (decrease) of Δ_{trig} of CoO_6 octahedra by reducing film thickness (by helium implantation). Consequently, the original T_N of 16 K in $\text{Cu}_3\text{Co}_2\text{SbO}_6$ was modulated from 22.7 K to 7.8 K, depending on the direction and the magnitude of the applied stretching. The modulation of T_N is as large as 90 % of the original T_N , indicating a strong correlation between Δ_{trig} and the stability of classical antiferromagnetic ground states. Our findings imply the possibility of a genuine spin liquid state if more stretching along the out-of-plane direction can be applied on $\text{Cu}_3\text{Co}_2\text{SbO}_6$.

II. ORBITAL STRUCTURE OF Co^{2+} ION IN HONEYCOMB COBALTATES

We first compare Co L -edge XAS of bulk-like 20 u.c. $\text{Cu}_3\text{Co}_2\text{SbO}_6$ film with that of $\text{Na}_3\text{Co}_2\text{SbO}_6$ film to elucidate the rather controversial relationship between orbital structures and distorted local CoO_6 octahedra in layered honeycomb cobaltates. Note that $\text{Na}_3\text{Co}_2\text{SbO}_6$ has an almost identical local structure of CoO_6 octahedra to $\text{Cu}_3\text{Co}_2\text{SbO}_6$, except for its smaller trigonal distortion (Fig. S1 in Ref. [36]). Considering crystal fields only from O^{2-} ions, we can expect positive Δ_{trig} with a lower energy of a_{1g} orbitals than e_g^π orbitals in both compounds (Fig. S2 in Ref. [36]), as the octahedra are compressed in the out-of-plane direction [Fig. 1(a)]. However, previous theoretical and experimental research on $\text{Na}_3\text{Co}_2\text{SbO}_6$ suggested the negative value of Δ_{trig} [23,37]. It has been attributed to that the size of the negative crystal field

from Sb^{5+} ions is larger than the size of the positive crystal field from O^{2-} ions (Fig. S2 in Ref. [36]).

Despite those predictions for Δ_{trig} , the $\text{Cu}_3\text{Co}_2\text{SbO}_6$ displayed a notably larger X-ray linear dichroism (XLD) in Co L_3 -edge spectra than $\text{Na}_3\text{Co}_2\text{SbO}_6$, implying a more dominant role of O^{2-} than Sb^{5+} ions in Δ_{trig} and the positive sign in total Δ_{trig} . Figures 2(a) and 2(b) exhibit the normalized isotropic XAS, $I_{\text{iso}} = (2I_{\perp z} + I_{\parallel z}) / 3$, and XLD, $I_{\text{XLD}} = I_{\perp z} - I_{\parallel z}$, at the Co L_3 edges for $\text{Cu}_3\text{Co}_2\text{SbO}_6$ and $\text{Na}_3\text{Co}_2\text{SbO}_6$, respectively. Here, $I_{\perp z}$ ($I_{\parallel z}$) denotes the XAS spectra with the incident polarization (denoted as \mathbf{E}) of light perpendicular (parallel) to the out-of-plane direction. We changed the polarization of the incident X-ray with a fixed incident angle α of 70° (Fig. S3 in Ref. [36]). From this experimental geometry, the spectra for the polarization were obtained by using the formula, $I_{\perp z} = I_p$ and $I_{\parallel z} = [I_s - I_p \cos^2(\alpha)] / \sin^2(\alpha)$, where I_p (I_s) are the measured intensities with p (s) polarization. The I_{iso} spectra at the Co L_3 edge of both compounds are nearly identical and resemble the well-known spectra of Co^{2+} ions [38]. The major difference in those spectra is that the I_{XLD} of $\text{Cu}_3\text{Co}_2\text{SbO}_6$ is roughly two times larger than that of $\text{Na}_3\text{Co}_2\text{SbO}_6$, indicating a larger magnitude of Δ_{trig} [39]. This result contrasts with the previous theoretical predictions which suggested a dominant Sb^{5+} crystal field and a negative Δ_{trig} . If Δ_{trig} were negative in layered honeycomb cobaltates, a more distortion in octahedra in $\text{Cu}_3\text{Co}_2\text{SbO}_6$ than $\text{Na}_3\text{Co}_2\text{SbO}_6$ would reduce the overall magnitude of Δ_{trig} with a larger positive crystal field from O^{2-} . The comparison between these two similar compounds underlines the dominant influence of the O^{2-} crystal field and supports a positive Δ_{trig} in layered honeycomb cobaltates (Fig. S2 in Ref. [36]). For estimating the magnitude of Δ_{trig} , the crystal field multiplet calculations were conducted using the quantum many-body script language, Quancy [40] with Crispy interface [41]. Even in the multiplet calculations, simulations with $\Delta_{\text{trig}} = 37.8$ meV (25.1 meV) are good agreements with the experimental I_{XLD} of $\text{Cu}_3\text{Co}_2\text{SbO}_6$ ($\text{Na}_3\text{Co}_2\text{SbO}_6$) film [Figs. 2(c) and 2(d)] and assist the above qualitative analysis.

The polarization-dependent O K -edge spectra further clarify unoccupied e_g^π orbitals and positive Δ_{trig} in the layered honeycomb cobaltates. The Co^{2+} ions in layered honeycomb cobaltates exhibit high spin d^7 configurations. Therefore, in O K -edge XAS of $\text{Cu}_3\text{Co}_2\text{SbO}_6$ and $\text{Na}_3\text{Co}_2\text{SbO}_6$ [Figs. 2(d)-2(f)], the lowest energy peak near 531 eV can be assigned to O $2p$ - Co t_{2g} hybridized state, while the multiple-peak features at higher energies are associated with O $2p$ orbitals hybridized with unoccupied Co e_g^σ and Cu $3d$ orbitals (Fig. S4 in Ref. [36]) [42-

46]. Given that trigonal distortion splits only the t_{2g} orbitals, we focused on polarization dependence in the lowest peak. In the O K edge, $I_{\perp z}$ ($I_{\parallel z}$) of the peak is proportional to the averaged interatomic matrix element V_{pd}^2 between Co t_{2g} orbitals and O $2p$ orbitals perpendicular (parallel) to the out-of-plane direction. Consequently, the relative intensity between $I_{\perp z}$ and $I_{\parallel z}$ is sensitive to whether the orbital character of the unoccupied t_{2g} orbital is mainly a_{1g} or e_g^π . The intensity ratio, $I_{\perp z} / I_{\parallel z}$, for the a_{1g} orbital character is calculated to be 0.25 in undistorted cubic octahedra and is expected to be less than 0.25 in the presence of trigonal distortions. That for e_g^π symmetry, on the other hand, is expected to be 1 in undistorted cubic octahedra and larger than 1 with trigonal distortion [43]. Therefore, if those cobaltates had a negative Δ_{trig} and unoccupied a_{1g} orbitals as predicted, we would observe a strong suppression in Co t_{2g} peak intensity in $I_{\perp z}$ compared to $I_{\parallel z}$ spectra. However, both compounds show enhancement of the peak intensity in $I_{\perp z}$ than in $I_{\parallel z}$, unambiguously indicating that the unoccupied e_g^π orbitals are dominant and that Δ_{trig} is indeed positive.

III. STRAIN ENGINEERING IN $\text{Cu}_3\text{Co}_2\text{SbO}_6$ HETEROSTRUCTURE

By utilizing our heterostructure geometry, we have successfully controlled the crystal structure and Δ_{trig} of $\text{Cu}_3\text{Co}_2\text{SbO}_6$ thin films. Figure 3(a) exhibits X-ray diffraction (XRD) θ - 2θ scan near the (008) peak of $\text{Cu}_3\text{Co}_2\text{SbO}_6$ film with 20 u.c. and 3 u.c. thickness. The (008) peak of 3 u.c. $\text{Cu}_3\text{Co}_2\text{SbO}_6$ film shifts to a higher angle than that of 20 u.c. $\text{Cu}_3\text{Co}_2\text{SbO}_6$ film, indicating reduced out-of-plane lattice constant, c^* ($c^* = c \sin(\beta)$ in lattice parameter) with thickness [33]. As shown in Fig. 3(b), c^* is quickly relaxed to its bulk value with increasing thickness due to the large lattice mismatch (+ 4.3 %) between ZnO and $\text{Cu}_3\text{Co}_2\text{SbO}_6$ (Fig. S5 in Ref. [36]). Reciprocal space mapping (RSM) data and q_x profiles [Figs. 3(c) and 3(d)] of the $\text{Cu}_3\text{Co}_2\text{SbO}_6$ (606) plane further demonstrates that the q_x value for the 3 u.c. film is smaller than that of the 20 u.c. film, indicative of an in-plane elongation. Based on these findings, we conclude that, despite the significant lattice mismatch, a tensile strain is indeed imparted upon the ultrathin $\text{Cu}_3\text{Co}_2\text{SbO}_6$ films. To increase c^* , on the other hand, we adopted helium implantation as helium atoms in matter induce c^* expansion with epitaxially locked in-plane lattice constants [34,35]. As we increased the dose of helium ions, the (004) peak of

$\text{Cu}_3\text{Co}_2\text{SbO}_6$ films shifted to a lower angle, in consistent with increased c^* [Figs. 3(e) and 3(f)]. Same as thickness-controlled films, we obtained RSM and q_x profiles of the $\text{Cu}_3\text{Co}_2\text{SbO}_6$ (606) plane for the He $3.6 \times 10^{15} \text{ cm}^{-2}$ implanted film [Figs. 3(g) and 3(h)]. As we expected, helium implantation barely modulates in-plane lattice constant compared to pristine $\text{Cu}_3\text{Co}_2\text{SbO}_6$ due to its locked lattice by neighboring unit cells. Full RSM images for each sample are shown in Fig. S6 in Ref [36].

The observed decrease (increase) of c^* in $\text{Cu}_3\text{Co}_2\text{SbO}_6$ films indeed reinforces (undermines) the trigonal distortion of the octahedra and Δ_{trig} . Figure 4(a) exhibits the evolution of I_{XLD} of Co L_3 edge with thickness and He ion implantation. I_{XLD} of 3 u.c. $\text{Cu}_3\text{Co}_2\text{SbO}_6$ film shows an overall enhancement compared to the 20 u.c. $\text{Cu}_3\text{Co}_2\text{SbO}_6$ film, indicating an increased Δ_{trig} [Fig. 4(a), left]. The He $3.6 \times 10^{15} \text{ cm}^{-2}$ implanted $\text{Cu}_3\text{Co}_2\text{SbO}_6$ films, in contrast, exhibit smaller I_{XLD} relative to the pristine $\text{Cu}_3\text{Co}_2\text{SbO}_6$ film [Fig. 4(a), right], indicating a decreased Δ_{trig} . Figure 4(b) shows the absolute area of XLD, $I_{|XLD|}$, in each stretched-thin film, which roughly represents the relative magnitude of Δ_{trig} [39], as well as simulated Δ_{trig} , which reproduced experimental I_{XLD} (Fig. S7 in Ref. [36]). Notably, $I_{|XLD|}$ of both the 3 u.c. and the He $3.6 \times 10^{15} \text{ cm}^{-2}$ implanted film is increased (reduced) to approximately 13 % (33 %) of the original value in the bulk-like $\text{Cu}_3\text{Co}_2\text{SbO}_6$, demonstrating capabilities of heterostructures for the direct control of Hamiltonian parameters.

IV. MODULATION OF THE NEEL TEMPERATURE INDUCED BY STRAIN ENGINEERING

To investigate the effect of the Δ_{trig} on its magnetic ground state, we conducted spectroscopic ellipsometry to detect T_N in strained $\text{Cu}_3\text{Co}_2\text{SbO}_6$ films. The previous research on $\text{Cu}_3\text{Co}_2\text{SbO}_6$ has shown a peculiar spin-exciton coupling that induces a distinct kink at T_N in a raw ellipsometric parameter Ψ , where $\tan\Psi$ is the intensity ratio between reflected p - and s -polarized light at the exciton peak energy of $\sim 4 \text{ eV}$ (Fig. S8 in Ref. [36]). Therefore, we fixed the photon energy at the resonant frequency of the exciton and obtained temperature-dependent Ψ as shown in Figs. 5(a)-5(f). Note that conventional magnetometry experiments make it difficult to detect T_N of ultrathin film owing to its extremely small volume and large paramagnetic/diamagnetic backgrounds from substrates, defects, and equipment environment (Fig. S9 in Ref. [36]). This optical detection of T_N is not only sufficiently sensitive for ultrathin

films but also free from any paramagnetic and diamagnetic backgrounds as no external magnetic field is required. Figure 5(a) shows $\Psi(T)$ of 20 u.c. $\text{Cu}_3\text{Co}_2\text{SbO}_6$ thin film. Even without complicated model fitting, we observed a clear kink at ~ 16 K in the raw ellipsometry parameter, which is consistent with T_N observed in conventional magnetometry experiments.

The strain engineering on $\text{Cu}_3\text{Co}_2\text{SbO}_6$ films and the resultant change in Δ_{trig} induced a massive modulation in T_N . Figures 5(a)-5(f) exhibit optical parameter Ψ of strained $\text{Cu}_3\text{Co}_2\text{SbO}_6$ thin films as a function of T . While T_N of the 3 u.c. $\text{Cu}_3\text{Co}_2\text{SbO}_6$ film with a larger Δ_{trig} is shifted to $22.7 \text{ K} \pm 1.8 \text{ K}$ [Fig. 5(c)], T_N in the He $3.6 \times 10^{15} \text{ cm}^{-2}$ $\text{Cu}_3\text{Co}_2\text{SbO}_6$ films with a reduced Δ_{trig} is suppressed to $7.8 \text{ K} \pm 1 \text{ K}$ [Fig. 5(f)]. The reduced T_N in helium-implanted films can hardly be attributed to any extrinsic origins such as impurity formation, as it recovered to the original value of 16 K with the removal of the helium ions through mild thermal annealing (Fig. S10 in Ref. [36]) [35]. Figure 5(g) is a summary of our discovery of strong positive correlations between Δ_{trig} and T_N in layered honeycomb cobaltates. Interestingly, although the $\text{Na}_3\text{Co}_2\text{SbO}_6$ has a different space group ($C 2/m$) [47] compared to $\text{Cu}_3\text{Co}_2\text{SbO}_6$ ($C 2/c$) [31], it follows the same relationship between Δ_{trig} and T_N observed in $\text{Cu}_3\text{Co}_2\text{SbO}_6$ films, as highlighted by a star in Fig. 5(g). It is strong evidence that reducing Δ_{trig} in CoO_6 octahedra is indeed a key to destabilizing classical ground states in layered honeycomb cobaltates.

V. SUMMARY AND DISCUSSION

Our findings above have testified to the effectiveness of strain engineering in heterostructures to destabilize unsought long-range ordering in spin liquid candidates. While previous studies in bulk have predominantly focused on the observation of fluctuating spin-disordered phases in response to external magnetic fields [15,48-50], our approach focused on direct manipulation of the spin Hamiltonian parameters. We believe this rather unexplored research direction could allow us to observe a new side of this notoriously elusive quantum phase of matter.

For example, strain-dependent T_N observed here can help to determine the effect of hopping integral for spin exchange interaction in cobalt-based honeycomb oxides. Several theoretical studies have raised questions about the effect of Co-Co direct spin-exchange interaction, which was neglected in the original calculation in high-spin d^7 compounds. In

particular, the direct hopping integral becomes the dominant one compared to the ligand-mediated hopping when the Co-Co bond length is small enough like in $\text{BaCo}_2(\text{AsO}_4)_2$ [51,52]. This complexity of energy hierarchy in tight-binding Hamiltonian is important in Kitaev physics as the inclusion of direct hopping integral results in isotropic or XXZ-type spin Hamiltonian in honeycomb cobaltates [52-54]. In the case of thickness-controlled films, the in-plane lattice stretching is clearly shown in Fig. 3(d). This stretching leads to an elongation of the Co-Co bond length, resulting in a decrease of direct spin exchange interaction. Therefore, if this direct exchange interaction is dominant in $\text{Cu}_3\text{Co}_2\text{SbO}_6$, we would expect to see a decrease of T_N in 3 u.c. $\text{Cu}_3\text{Co}_2\text{SbO}_6$ film, in opposed to our experiment in Fig. 5(c). Therefore, our observation implies that a more important factor in controlling the magnetic ground state is Δ_{trig} than direct exchange hopping at least in honeycomb cobaltates $\text{Cu}_3\text{Co}_2\text{SbO}_6$. The difference between $\text{BaCo}_2(\text{AsO}_4)_2$ and $\text{Cu}_3\text{Co}_2\text{SbO}_6$ might be attributed to different bond-length (3.11 Å for $\text{Cu}_3\text{Co}_2\text{SbO}_6$ and 2.9 Å for $\text{BaCo}_2(\text{AsO}_4)_2$) as the previous theory mentioned [52].

Our results motivate further studies on layered honeycomb cobaltate heterostructures to realize a genuine quantum spin liquid state. As several theoretical studies have pointed out, [8,27,55,56] fine-tuning of spin Hamiltonian seems to be inevitable to realize an otherwise fragile spin liquid state. However, challenges arise from the low volume of ultrathin film and/or helium-induced paramagnetic impurities, which hinder conventional magnetic susceptibility measurement and complicate the investigation of antiferromagnetic ordering in Kitaev QSL candidates. The obvious future research would be identifying substrates and buffer layers that can not only facilitate larger compressive strain but also potentially applicable to other cobaltates like $\text{Na}_3\text{Co}_2\text{SbO}_6$. Since $\text{Na}_3\text{Co}_2\text{SbO}_6$ inherently possesses a smaller Δ_{trig} than $\text{Cu}_3\text{Co}_2\text{SbO}_6$, the complete suppression of antiferromagnetic ordering can be achieved via moderate compressive strain. While searching for evidence of Kitaev QSL will be notoriously challenging in heterostructures, a few recent theoretical suggestions based on electrical measurement, spintronics as well as inelastic tunneling experiments can be applicable to our systems [57-60].

In conclusion, we have demonstrated the control of the Δ_{trig} of $\text{Cu}_3\text{Co}_2\text{SbO}_6$, a promising candidate of Kitaev QSL, and the subsequent destabilization of its classical antiferromagnetic ground state. Our lattice-engineered $\text{Cu}_3\text{Co}_2\text{SbO}_6$ system opens the pathway to tailor the spin interactions in layered honeycomb cobaltate systems, offering valuable

insights into the underlying physics of Kitaev materials.

VI. MATERIALS AND METHODS

A. Sample preparation

The $\text{Na}_3\text{Co}_2\text{SbO}_6$ and $\text{Cu}_3\text{Co}_2\text{SbO}_6$ thin films were synthesized using pulsed laser deposition. For high-quality thin films, the O-faced ZnO [0001] substrates were annealed for 2 hours at 1100 °C in ambient pressure. The $\text{Na}_3\text{Co}_2\text{SbO}_6$ and $\text{Cu}_3\text{Co}_2\text{SbO}_6$ targets were synthesized using the solid-state reaction method with the reported recipe of polycrystalline powder [31,47]. The optimized growth conditions of $\text{Na}_3\text{Co}_2\text{SbO}_6$ were as follows: substrate temperature $T = 625$ °C, oxygen partial pressure $P = 1$ mTorr, the energy of the KrF Excimer laser ($\lambda = 248$ nm) $E = 1.1$ J / cm², the laser repetition rate is 10 Hz, and the distance between the target and substrate was set at 50 mm. The cooling process was performed under the same as grown pressure after the deposition was completed. For the XAS experiment, 40 u.c. (21 nm) thickness $\text{Na}_3\text{Co}_2\text{SbO}_6$ films were used. For $\text{Cu}_3\text{Co}_2\text{SbO}_6$, optimized growth conditions were a substrate temperature $T = 800$ °C, oxygen partial pressure $P = 10$ mTorr, the energy of the KrF Excimer laser ($\lambda = 248$ nm) $E = 1.3$ J / cm², laser repetition rate is 10 Hz, and the distance between the target and substrate was set at 50 mm. The cooling process was performed under the same as grown pressure after the deposition was completed. For the helium ion implantation, 20 u.c. (23 nm) thickness $\text{Cu}_3\text{Co}_2\text{SbO}_6$ films were used.

B. Helium ion implantation

Helium ions were implanted into 20 u.c. $\text{Cu}_3\text{Co}_2\text{SbO}_6$ thin films using a metal ion implanter at in Korean Multi-Purpose Accelerator Complex (KOMAC). Helium ion is injected into each sample with 10 keV energy at room T and vacuum environment. Each flux density of helium ion was 1.7×10^{15} cm⁻², 2.6×10^{15} cm⁻², and 3.6×10^{15} cm⁻². To prevent the damage of films due to high-energy ion beam, a 48 nm-thick gold layer was deposited using thermal evaporation. For the XAS measurements, the gold layer was peeled off by Kapton tape. Details about the thickness of the gold layer and average helium ion density in the thin film are determined by Stopping and Range of Ions in Matter / Transport of Ions in Matter (SRIM/TRIM) Monte Carlo simulation (Fig. S11 in Ref. [36]).

C. Characterization of lattice structure

To characterize the crystal structure of $\text{Cu}_3\text{Co}_2\text{SbO}_6$ thin films, high-resolution XRD data for each $\text{Cu}_3\text{Co}_2\text{SbO}_6$ thin film were collected by using D8 Advance High-Resolution X-ray Diffractometer (Bruker) with Cu $K\text{-}\alpha 1$ wavelength. 0D Lynxeye detector is used in θ - 2θ scan, which has 0.01° increment with a scan speed of 0.5 sec/step. Each scan has range from 60° to 80° for thickness-dependent $\text{Cu}_3\text{Co}_2\text{SbO}_6$ thin films and from 25° to 40° for helium-implanted thin film. We used the (008) diffraction peak to determine the lattice constant c^* of thickness-controlled $\text{Cu}_3\text{Co}_2\text{SbO}_6$ to avoid overlapping with ZnO substrate peak. For a detailed structural analysis, RSM data of the $\text{Cu}_3\text{Co}_2\text{SbO}_6$ (606) peak and the ZnO (114) peak were conducted on each $\text{Cu}_3\text{Co}_2\text{SbO}_6$ thin film at the 3A Hard X-ray Scattering Beamline in PLS-II of the Pohang Accelerator Laboratory.

D. X-ray absorption spectroscopy

The XAS measurements were conducted at the 2A magnetic spectroscopy beamline in PLS-II of the Pohang Accelerator Laboratory. Those were performed in a zero-applied magnetic field, in a vacuum with a pressure lower than 2×10^{-9} torr at room temperature, and in total electron yield mode. To prevent the charging effect, we bridged four edges of film surfaces and a copper holder with silver paint. Since the implanted helium ions can escape from the samples in high temperature [35], the sample temperature was maintained at room temperature with nitrogen gas during the vacuum baking process. We acquired XAS spectra at the Co L edges and O K edge with an energy resolution of 0.1 and 0.2 eV, respectively. To compare the XAS spectra of different films, they are normalized based on the total area of the isotropic spectra in the range of 770 eV to 790 eV for Co L_3 edge and of 785 eV to 805 eV for Co L_2 edge (Fig. S14 in Ref. [36]). The absolute area of XLD, $I_{|XLD|}$ is determined by integrating within the range of 775 eV to 785 eV for Co L_3 edge in XLD spectra. Additional XAS data for each thickness-controlled and helium ion implanted $\text{Cu}_3\text{Co}_2\text{SbO}_6$ thin films are shown in the supplemental material (Figs. S12-S15 in Ref. [36]).

E. Crystal field multiplet calculation for Co L -edge XAS

The crystal field multiplet calculations were conducted using the quantum many-body script language, Quanta [40]. The user interface called Crispy is used to generate input files consisting of Slater-Condon and crystal field parameters and to visualize the simulated spectra of I_{iso} and I_{XLD} [41]. With C_{3v} site symmetry, the trigonal field parameters $10Dq$, D_σ , and D_τ

were estimated by simulating the experimental L_3 -edge spectra. Note that both D_{3d} and C_{3v} have the same trigonal symmetry. The Slater-Condon parameters for electron-electron repulsion (F^k_{dd}, F^k_{pd}) and exchange (G^k_{pd}, G^k_{dd}) were scaled down by multiplying a factor of 80% to compensate for the electronic delocalization in $3d$ orbital [38]. The spin-orbit coupling parameters of $2p$ and $3d$ are evaluated as 9.745 eV and 0.066 eV, respectively. To reproduce the exact shape of each spectrum, 0.4 eV Gaussian broadening is adopted. The Lorentzian broadening for L_2 edge and L_3 edge are selected as 0.5 eV and 0.6 eV, respectively.

F. Ellipsometry

We measured the ellipsometry parameters Ψ and Δ of $\text{Cu}_3\text{Co}_2\text{SbO}_6$ thin films on ZnO substrate by using an M-2000 ellipsometer (J. A. Woolam Co.). $\tan\Psi$ is the amplitude ratio of the reflected p - and s -waves, while Δ represents the phase shift between the two waves. For all samples Ψ and Δ were obtained across an energy range from 0.74 to 6.46 eV (5900 to 52000 cm^{-1}) at an incident angle of 60° (80° for 3 u.c. $\text{Cu}_3\text{Co}_2\text{SbO}_6$ for adapting good sensitivity) and over a temperature range of 6 to 300 K. Each data collection lasted 200 seconds. For low- T measurement, the window effect was calibrated by using a 25 nm SiO_2 / Si wafer. To prevent degradation of the sample implanted helium ions, we avoided baking out the chamber. The base pressure has remained below 1×10^{-8} Torr. All samples were mounted using carbon tape to oxygen-free copper cones.

G. Magnetic susceptibility

Field-cooled magnetization curves with respect to T for $\text{Cu}_3\text{Co}_2\text{SbO}_6$, $\text{Na}_3\text{Co}_2\text{SbO}_6$, and He-implanted $\text{Cu}_3\text{Co}_2\text{SbO}_6$ thin films on ZnO substrate were measured by superconducting quantum interference device (Quantum Design). The mass and dimension of each sample were precisely investigated as 13.6 mg and $3.3 \text{ mm} \times 2.5 \text{ mm}$. We measured magnetization with the direction of ZnO (110) Also, to compensate paramagnetic signal from the substrate, the magnetization of ZnO with the same dimension, of 13.6 mg was obtained. During measurements, samples are attached to a quartz plate mounted by GE varnish. All magnetic susceptibility data were calculated by substituting the diamagnetic signal in the substrate with mass-normalization.

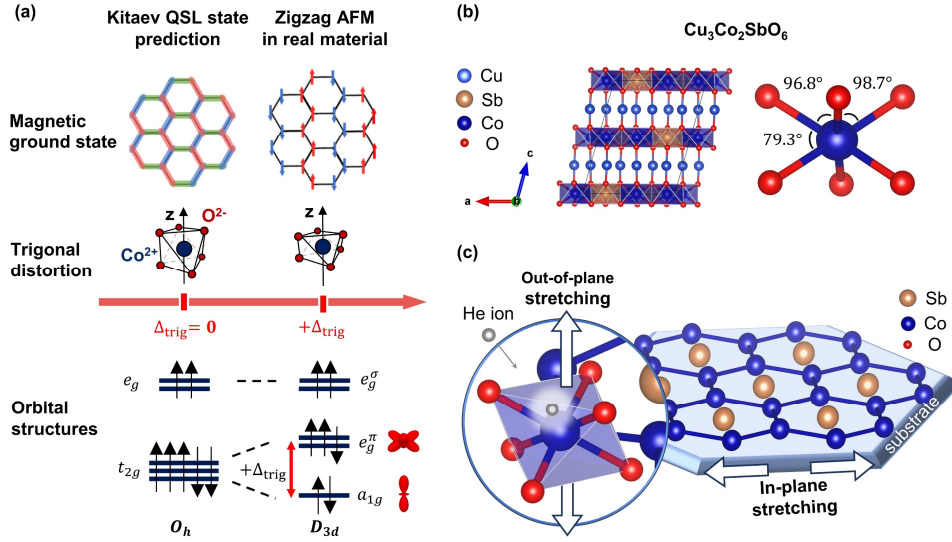


FIG. 1. (a) Relationship among local trigonal distortion of CoO_6 octahedra, orbital structures, and the magnetic ground state of $\text{Cu}_3\text{Co}_2\text{SbO}_6$. The t_{2g} orbital in the O_h system split into e_g^π orbital and a_{1g} orbital by trigonal distortion of CoO_6 octahedra with D_{3d} symmetry. The energy difference between the e_g^π and a_{1g} level is defined by the Δ_{trig} . According to theoretical predictions, the Kitaev QSL state could be realized with decreasing Δ_{trig} in the layered honeycomb cobaltates. (b) The crystal structure of layered honeycomb cobaltate $\text{Cu}_3\text{Co}_2\text{SbO}_6$ and O-Co-O bond angles of CoO_6 octahedra, indicating compressed octahedra along the out-of-plane direction [\mathbf{z} -axis in Fig. 1(a)]. (c) Two ways for modulating Δ_{trig} of CoO_6 octahedra. While helium implantation would decrease Δ_{trig} by stretching the octahedra along the out-of-plane direction, the strain imposed on the ultrathin film through the substrate would increase Δ_{trig} by stretching the octahedra in the in-plane direction.

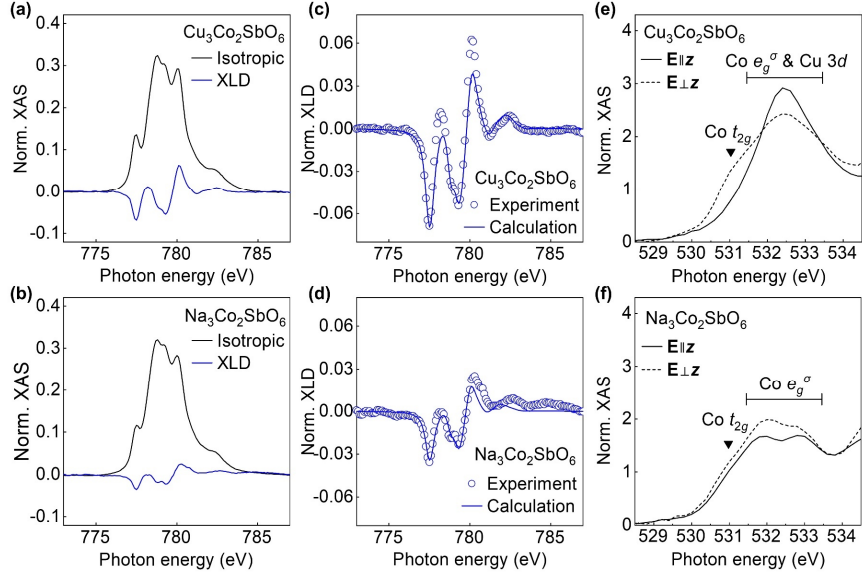


FIG. 2. Isotropic XAS, $I_{iso} = (2I_{\perp z} + I_{\parallel z}) / 3$, and XLD, $I_{XLD} = I_{\perp z} - I_{\parallel z}$, of Co L_3 edge in (a) $\text{Cu}_3\text{Co}_2\text{SbO}_6$ and (b) $\text{Na}_3\text{Co}_2\text{SbO}_6$. $I_{\perp z}$ ($I_{\parallel z}$) is normalized XAS signals with each polarization, \mathbf{E} field perpendicular (parallel) to the out-of-plane direction. The experimental XLD data (open circles) and the simulation from crystal field multiplet calculation (solid lines) of (c) $\text{Cu}_3\text{Co}_2\text{SbO}_6$ and (d) $\text{Na}_3\text{Co}_2\text{SbO}_6$. Based on calculations within trigonal symmetry, the trigonal field strength is deduced to be 37.8 and 25.1 meV for $\text{Cu}_3\text{Co}_2\text{SbO}_6$, and $\text{Na}_3\text{Co}_2\text{SbO}_6$, respectively. The polarization-dependent O K -edge XAS for (e) $\text{Cu}_3\text{Co}_2\text{SbO}_6$ and (f) $\text{Na}_3\text{Co}_2\text{SbO}_6$. Individual peaks can be assigned to unoccupied O $2p$ orbitals hybridized with Co $3d$ t_{2g} and e_g orbitals. In $\text{Cu}_3\text{Co}_2\text{SbO}_6$, the additional peak near 532.5 eV is the known transition from O $1s$ to O $2p - \text{Cu } 3d$ hybridized state in Cu^+ valence systems. In both compounds, the intensity of the Co t_{2g} peak is enhanced in $I_{\perp z}$, indicating dominant e_g^π symmetry in the unoccupied state of the Co^{2+} ion.

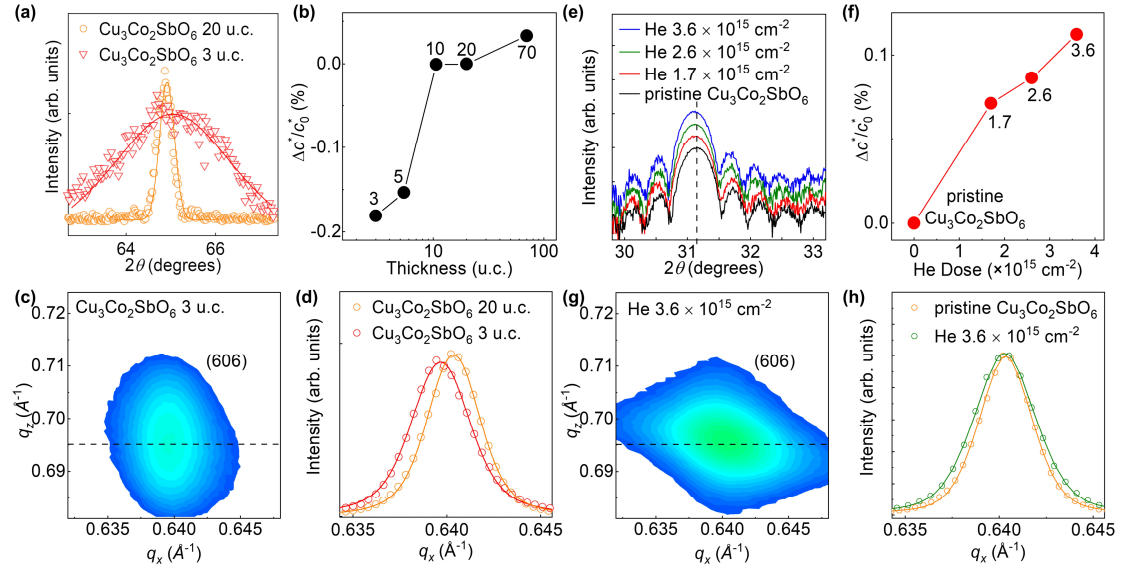


FIG. 3. (a) XRD θ - 2θ scan of near the $\text{Cu}_3\text{Co}_2\text{SbO}_6$ (008) peak of 3 u.c. and 20 u.c. film in linear scale. The tensile strain from the ZnO substrate induced expansion of the out-of-plane lattice parameter, resulting in a shift of the (008) peak of $\text{Cu}_3\text{Co}_2\text{SbO}_6$ to a higher angle. (b) The change of out-of-plane lattice parameter, $\Delta c^*/c_0^*$ as a function of thickness in $\text{Cu}_3\text{Co}_2\text{SbO}_6$ thin film. Δc^* was calculated with respect to c^* of 20 uc film, c_0^* . Due to the huge lattice mismatch between ZnO and $\text{Cu}_3\text{Co}_2\text{SbO}_6$, the tensile strain rapidly relaxed as the thickness of the film increased. (c) RSM and (d) q_x profile for (606) plane of 3 u.c. $\text{Cu}_3\text{Co}_2\text{SbO}_6$ thin film. A smaller q_x value in 3 u.c. thin film than that in 20 u.c. thick film indicates the in-plane stretching in ultrathin film (Fig. S6 in Ref. [36]). (e) XRD θ - 2θ scan and (f) $\Delta c^*/c_0^*$ of $\text{Cu}_3\text{Co}_2\text{SbO}_6$ film as a function of doses of helium ion. The (004) peak of $\text{Cu}_3\text{Co}_2\text{SbO}_6$ shifts to lower angles with increased dosed helium ions, indicating out-of-plane stretching of the lattice. (g) RSM image and (h) q_x profile of the $\text{He } 3.6 \times 10^{15} \text{ cm}^{-2}$ implanted $\text{Cu}_3\text{Co}_2\text{SbO}_6$ thin film (Fig. S6 in Ref. [36]). The peak from helium implanted film maintains the same q_x position as that of the pristine 20 u.c. film due to its epitaxially locked in-plane lattice constants.

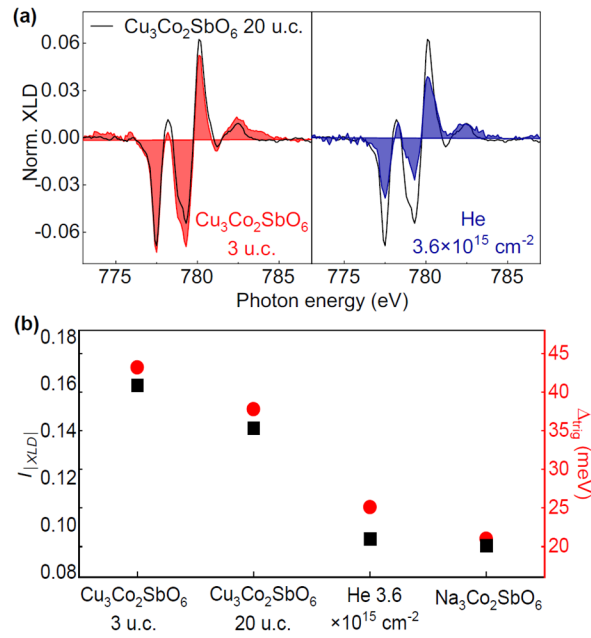


FIG. 4. (a) I_{XLD} of Co L_3 edge for 3 u.c. $\text{Cu}_3\text{Co}_2\text{SbO}_6$ thin film (left) and He $3.6 \times 10^{15} \text{ cm}^{-2}$ implanted $\text{Cu}_3\text{Co}_2\text{SbO}_6$ thin film (right). For comparison, I_{XLD} of 20 u.c. $\text{Cu}_3\text{Co}_2\text{SbO}_6$ is also shown as black lines. Films with more out-of-plane stretching showed decreased XLD signals, while films with increased in-plane stretching showed larger XLD signals. This observation clearly indicates the successful modulation of the Δ_{trig} . (b) The absolute area of XLD, $I_{|XLD|}$, and Δ_{trig} deduced from the crystal field multiplet calculation of XLD spectra for 3 u.c. $\text{Cu}_3\text{Co}_2\text{SbO}_6$ film, 20 u.c. $\text{Cu}_3\text{Co}_2\text{SbO}_6$ film, He $3.6 \times 10^{15} \text{ cm}^{-2}$ implanted $\text{Cu}_3\text{Co}_2\text{SbO}_6$ film, and $\text{Na}_3\text{Co}_2\text{SbO}_6$ film.

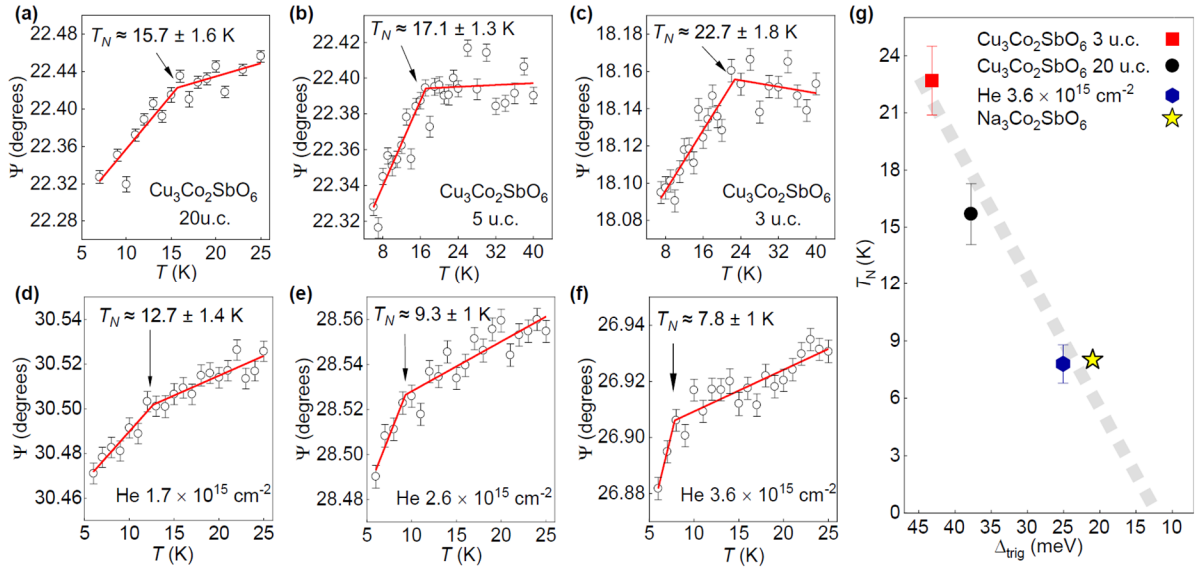


FIG. 5. The T -dependent ellipsometric parameter Ψ (open circles) at exciton peak energies, which can be used to detect T_N via spin-exciton coupling: The red solid lines are piecewise function fitting for (a) 20 u.c. $\text{Cu}_3\text{Co}_2\text{SbO}_6$ thin film with the $T_N \sim 15.7 \pm 1.6$ K, (b) 5 u.c. $\text{Cu}_3\text{Co}_2\text{SbO}_6$ thin film with the $T_N \sim 17.1 \pm 1.3$ K, (c) 3 u.c. $\text{Cu}_3\text{Co}_2\text{SbO}_6$ thin film with the $T_N \sim 22.7 \pm 1.8$ K, (d) He $1.7 \times 10^{15} \text{ cm}^{-2}$ implanted $\text{Cu}_3\text{Co}_2\text{SbO}_6$ with the $T_N \sim 12.7 \pm 1.4$ K, (e) He $2.6 \times 10^{15} \text{ cm}^{-2}$ implanted $\text{Cu}_3\text{Co}_2\text{SbO}_6$ with the $T_N \sim 9.3 \pm 1$ K, and (f) He $3.6 \times 10^{15} \text{ cm}^{-2}$ implanted $\text{Cu}_3\text{Co}_2\text{SbO}_6$ with the $T_N \sim 7.8 \pm 1$ K. Almost 90 % of modulation in T_N is achieved by in-plane and out-of-plane stretching of $\text{Cu}_3\text{Co}_2\text{SbO}_6$ films. (g) The Δ_{trig} versus T_N graph clearly visualizes strong positive correlations between those two parameters in the layered cobaltates. The grey dashed line is guided for eyes. Although $\text{Na}_3\text{Co}_2\text{SbO}_6$ has a different space group from $\text{Cu}_3\text{Co}_2\text{SbO}_6$, it follows the same relationship between T_N and Δ_{trig} found in $\text{Cu}_3\text{Co}_2\text{SbO}_6$, as highlighted by a star (Fig. S9 in Ref. [36]). Therefore, the Δ_{trig} can be considered the key parameter for destabilizing classical magnetic ground state in the layered honeycomb cobaltates.

ACKNOWLEDGMENTS

We extend our sincere gratitude to F. M. F. de Groot for his invaluable discussions. This work was mainly supported by the National Research Foundation (NRF) of Korea funded by the Ministry of Science and ICT (Grant No. NRF-2020R1C1C1008734), under the ITRC (Information Technology Research Center) support program (IITP-2023-RS-2023-00259676) supervised by the IITP (Institute for Information & Communications Technology Planning & Evaluation), and by the MSIT and PAL, Korea. Experiments at PLS-II were supported in part by MSIT and POSTECH. The exceptional assistance provided by S.Y. Park and Y.H. Kim during the PLS-II experiments is gratefully acknowledged. The preparation of helium-implanted samples was supported by the KOMAC (Korea Multi-purpose Accelerator Complex) operation fund of KAERI (Korea Atomic Energy Research Institute) by MSIT. H.R. Jeon is acknowledged for helping helium implantation experiments. The M-2000 ellipsometer (J.A. Woolam Co.) for optical measurements was supported by the IBS Center for Correlated Electron Systems, Seoul National University. Deok-Yong Cho was supported by the National Research Foundation of Korea (Grant No. 2021R1A2C1004644), funded by the Korea government (MSIT). Jung-woo Yoo was supported by the NRF of Korea (Grant No. 2021R1A2C1008431). Jong Mok Ok was supported by the Nano & Material Technology Development Program through the National Research Foundation of Korea (NRF) funded by the Ministry of Science and ICT (RS-2023-00281839).

REFERENCES

- [1] P. W. Anderson, *Resonating valence bonds: A new kind of insulator?*, Mat. Res. Bull. **8**, 153 (1973).
- [2] P. W. Anderson, G. Baskaran, Z. Zou, and T. Hsu, *Resonating–valence-bond theory of phase transitions and superconductivity in La_2CuO_4 -based compounds*, Phys. Rev. Lett. **58**, 2790 (1987).
- [3] C. Broholm, R. Cava, S. Kivelson, D. Nocera, M. Norman, and T. Senthil, *Quantum spin liquids*, Science **367**, eaay0668 (2020).
- [4] L. Savary and L. Balents, *Quantum spin liquids: a review*, Rep. Prog. Phys. **80**, 016502 (2016).
- [5] Y. Zhou, K. Kanoda, and T.-K. Ng, *Quantum spin liquid states*, Rev. Mod. Phys. **89**, 025003 (2017).
- [6] A. Kitaev, *Anyons in an exactly solved model and beyond*, Annals of Physics **321**, 2 (2006).
- [7] J. Chaloupka, G. Jackeli, and G. Khaliullin, *Kitaev-Heisenberg model on a honeycomb lattice: possible exotic phases in iridium oxides A_2IrO_3* , Phys. Rev. Lett. **105**, 027204 (2010).
- [8] Y. Yamaji, T. Suzuki, T. Yamada, S. I. Suga, N. Kawashima, and M. Imada, *Clues and criteria for designing a Kitaev spin liquid revealed by thermal and spin excitations of the honeycomb iridate Na_2IrO_3* , Phys. Rev. B **93**, 174425 (2016).
- [9] Y. Singh, S. Manni, J. Reuther, T. Berlijn, R. Thomale, W. Ku, S. Trebst, and P. Gegenwart, *Relevance of the Heisenberg-Kitaev model for the honeycomb lattice iridates A_2IrO_3* , Phys. Rev. Lett. **108**, 127203 (2012).
- [10] H. Gretarsson, J. P. Clancy, X. Liu, J. P. Hill, E. Bozin, Y. Singh *et al.*, *Crystal-field splitting and correlation effect on the electronic structure of A_2IrO_3* , Phys. Rev. Lett. **110**, 076402 (2013).
- [11] M. Jenderka, J. Barzola-Quiquia, Z. Zhang, H. Frenzel, M. Grundmann, and M. Lorenz, *Mott variable-range hopping and weak antilocalization effect in heteroepitaxial Na_2IrO_3 thin films*, Phys. Rev. B **88**, 045111 (2013).
- [12] R. D. Johnson *et al.*, *Monoclinic crystal structure of α - RuCl_3 and the zigzag antiferromagnetic ground state*, Phys. Rev. B **92**, 235119 (2015).
- [13] Y. Kubota, H. Tanaka, T. Ono, Y. Narumi, and K. Kindo, *Successive magnetic phase transitions in α - RuCl_3 : XY-like frustrated magnet on the honeycomb lattice*, Phys. Rev. B **91**, 094422 (2015).
- [14] M. Majumder, M. Schmidt, H. Rosner, A. A. Tsirlin, H. Yasuoka, and M. Baenitz, *Anisotropic $\text{Ru}^{3+} 4d^5$ magnetism in the α - RuCl_3 honeycomb system: Susceptibility, specific heat, and zero-field NMR*, Phys. Rev. B **91**, 180401(R) (2015).
- [15] S.-H. Baek, S.-H. Do, K.-Y. Choi, Y. S. Kwon, A. U. B. Wolter, S. Nishimoto, J. vandenBrink, and B. Büchner, *Evidence for a field-induced quantum spin liquid in α - RuCl_3* , Phys. Rev. Lett. **119**, 037201 (2017).
- [16] A. Banerjee *et al.*, *Neutron scattering in the proximate quantum spin liquid α - RuCl_3* , Science **356**, 1055 (2017).
- [17] S.-H. Do *et al.*, *Majorana fermions in the Kitaev quantum spin system α - RuCl_3* , Nat. Phys. **13**, 1079 (2017).
- [18] H. Liu, J. Chaloupka, and G. Khaliullin, *Exchange interactions in d^5 Kitaev materials: From Na_2IrO_3 to α - RuCl_3* , Phys. Rev. B **105**, 214411 (2022).
- [19] R. Sano, Y. Kato, and Y. Motome, *Kitaev-Heisenberg Hamiltonian for high-spin d^7 Mott insulators*, Phys. Rev. B **97**, 014408 (2018).

- [20] H. Liu, *Towards Kitaev spin liquid in 3d transition metal compounds*, International Journal of Modern Physics B **35**, 2130006 (2021).
- [21] G. Jackeli and G. Khaliullin, *Mott insulators in the strong spin-orbit coupling limit: from Heisenberg to a quantum compass and Kitaev models*, Phys. Rev. Lett. **102**, 017205 (2009).
- [22] H. Liu and G. Khaliullin, *Pseudospin exchange interactions in d^7 cobalt compounds: Possible realization of the Kitaev model*, Phys. Rev. B **97**, 014407 (2018).
- [23] H. Liu, J. Chaloupka, and G. Khaliullin, *Kitaev Spin Liquid in 3d Transition Metal Compounds*, Phys. Rev. Lett. **125**, 047201 (2020).
- [24] E. Lefrançois *et al.*, *Magnetic properties of the honeycomb oxide $\text{Na}_3\text{Co}_2\text{TeO}_6$* , Phys. Rev. B **94**, 214416 (2016).
- [25] M. Songvilay *et al.*, *Kitaev interactions in the co honeycomb antiferromagnets $\text{Na}_3\text{Co}_2\text{SbO}_6$ and $\text{Na}_3\text{Co}_2\text{TeO}_6$* , Phys. Rev. B **102**, 224429 (2020).
- [26] X. Li *et al.*, *Giant Magnetic In-Plane Anisotropy and Competing Instabilities in $\text{Na}_3\text{Co}_2\text{SbO}_6$* , Phys. Rev. X **12**, 041024 (2022).
- [27] A. L. Sanders, R. A. Mole, J. Liu, A. J. Brown, D. Yu, C. D. Ling, and S. Rachel, *Dominant Kitaev interactions in the honeycomb materials $\text{Na}_3\text{Co}_2\text{SbO}_6$ and $\text{Na}_3\text{Co}_2\text{TeO}_6$* , Phys. Rev. B **106**, 014413 (2022).
- [28] E. Vavilova, T. Vasilchikova, A. Vasiliev, D. Mikhailova, V. Nalbandyan, E. Zvereva, and S. V. Streltsov, *Magnetic phase diagram and possible Kitaev-like behavior of the honeycomb-lattice antimonate $\text{Na}_3\text{Co}_2\text{SbO}_6$* , Phys. Rev. B **107**, 054411 (2023).
- [29] X. Zhang, Y. Xu, T. Halloran, R. Zhong, C. Broholm, R. Cava, N. Drichko, and N. Armitage, *A magnetic continuum in the cobalt-based honeycomb magnet $\text{BaCo}_2(\text{AsO}_4)_2$* , Nat. Mater. **22**, 58 (2023).
- [30] J.-Q. Yan, S. Okamoto, Y. Wu, Q. Zheng, H. D. Zhou, H. B. Cao, and M. A. McGuire, *Magnetic order in single crystals of $\text{Na}_3\text{Co}_2\text{SbO}_6$ with a honeycomb arrangement of $3d^7$ Co^{2+} ions*, Phys. Rev. Materials **3**, 074405 (2019).
- [31] J. Roudebush, N. H. Andersen, R. Ramlau, V. O. Garlea, R. Toft-Petersen, P. Norby, R. Schneider, J. Hay, and R. Cava, *Structure and Magnetic Properties of $\text{Cu}_3\text{Ni}_2\text{SbO}_6$ and $\text{Cu}_3\text{Co}_2\text{SbO}_6$ Delafossites with Honeycomb Lattices*, Inorg. Chem. **52**, 6083 (2013).
- [32] B. Kang *et al.*, arXiv preprint arXiv:2309.15753
- [33] J. Chakhalian, J. M. Rondinelli, J. Liu, B. A. Gray, M. Kareev, E. J. Moon, *et al.*, *Asymmetric Orbital-Lattice Interactions in Ultrathin Correlated Oxide Films*, Phys. Rev. Lett. **107**, 116805 (2011).
- [34] H. Guo *et al.*, *Strain doping: Reversible single-axis control of a complex oxide lattice via helium implantation*, Phys. Rev. Lett. **114**, 256801 (2015).
- [35] M. Brahlek *et al.*, *Emergent Magnetism with Continuous Control in the Ultrahigh-Conductivity Layered Oxide PdCoO_2* , Nano Lett. **23**, 7279 (2023).
- [36] See Supplementary Material at (DOI) for details of lattice and orbital structure analysis with strain-controlled $\text{Cu}_3\text{Co}_2\text{SbO}_6$ thin films and multiplet calculations for extracting trigonal crystal field strength.
- [37] M. van Veenendaal *et al.*, *Electronic structure of Co 3d states in the Kitaev material candidate honeycomb cobaltate $\text{Na}_3\text{Co}_2\text{SbO}_6$ probed with x-ray dichroism*, Phys. Rev. B **107**, 214443 (2023).
- [38] M. M. van Schooneveld, R. Kurian, A. Juhin, K. Zhou, J. Schlappa, V. N. Strocov, T. Schmitt, and F. M. F. de Groot, *Electronic Structure of CoO Nanocrystals and a Single Crystal Probed by Resonant X-ray Emission Spectroscopy*, J. Phys. Chem.

m. C **116**, 15218 (2012).

- [39] F. Bruno *et al.*, *Rationalizing strain engineering effects in rare-earth nickelates*, Phys. Rev. B **88**, 195108 (2013).
- [40] M. W. Haverkort, M. Zwierzycki, and O. K. Andersen, *Multiplet ligand-field theory using Wannier orbitals*, Phys. Rev. B **85**, 165113 (2012).
- [41] M. Retegan, (2019).
- [42] F. M. F. deGroot, M. Grioni, J. C. Fuggle, J. Ghijsen, G. A. Sawatzky, and H. Petersen, *Oxygen $1s$ x-ray-absorption edges of transition-metal oxides*, Phys. Rev. B **40**, 5715 (1989).
- [43] W. B. Wu, D. J. Huang, J. Okamoto, A. Tanaka, H. J. Lin, F. C. Chou, A. Fujimori, and C. T. Chen, *Orbital Symmetry and Electron Correlation in Na_xCoO_2* , Phys. Rev. Lett. **94**, 146402 (2005).
- [44] B. Kang *et al.*, *Honeycomb oxide heterostructure as a candidate host for a Kitaev quantum spin liquid*, Phys. Rev. B **107**, 075103 (2023).
- [45] M. Grioni, J. F. van Acker, M. T. Czyzyk, and J. C. Fuggle, *Unoccupied electronic structure and core-hole effects in the x-ray-absorption spectra of Cu_2O* , Phys. Rev. B **45**, 3309 (1992).
- [46] A. B. Gurevich, B. E. Bent, A. V. Teplyakov, and J. G. Chen, *A NEXAFS investigation of the formation and decomposition of CuO and Cu_2O thin films on $\text{Cu}(100)$* , Surface science **442**, L971 (1999).
- [47] C. Wong, M. Avdeev, and C. D. Ling, *Zig-zag Magnetic Ordering in Honeycomb-Layered $\text{Na}_3\text{Co}_2\text{SbO}_6$* , J. Solid State Chem. **243**, 18 (2016).
- [48] Z. Wang, S. Reschke, D. Hühvonen, S.-H. Do, K.-Y. Choi, M. Gensch, U. Nagel, T. Rößler, and A. Loidl, *Magnetic Excitations and Continuum of a Possibly Field-Induced Quantum Spin Liquid in $\alpha\text{-RuCl}_3$* , Phys. Rev. Lett. **119**, 227202 (2017).
- [49] J. Zheng *et al.*, *Gapless Spin Excitations in the Field-Induced Quantum Spin Liquid Phase of $\alpha\text{-RuCl}_3$* , Phys. Rev. Lett. **119**, 227208 (2017).
- [50] Y.-F. Jiang, T. P. Devereaux, and H.-C. Jiang, *Field-induced quantum spin liquid in the Kitaev-Heisenberg model and its relation to $\alpha\text{-RuCl}_3$* , Phys. Rev. B **100**, 165123 (2019).
- [51] T. Halloran *et al.*, *Geometrical frustration versus Kitaev interactions in $\text{BaCo}_2(\text{AsO}_4)_2$* , Proc. Natl. Acad. Sci. USA **120**, (2023). e2215509119.
- [52] X. Liu and H.-Y. Kee, *Non-Kitaev versus Kitaev honeycomb cobaltates*, Phys. Rev. B **107**, 054420 (2023).
- [53] S. M. Winter, *Magnetic couplings in edge-sharing high-spin d^7 compounds*, J. Phys. Mater. **5** (2022).
- [54] G. Lin *et al.*, *Field-induced quantum spin disordered state in spin-1/2 honeycomb magnet $\text{Na}_2\text{Co}_2\text{TeO}_6$ with small Kitaev interaction*, Nat. Commun. **12**, 5559 (2021).
- [55] S. M. Winter, Y. Li, H. O. Jeschke, and R. Valentí, *Challenges in design of Kitaev materials: Magnetic interactions from competing energy scales*, Phys. Rev. B **93**, 214431 (2016).
- [56] H. Liu, *Towards Kitaev Spin Liquid in 3d Transition Metal Compounds*, Int. J. Mod. Phys. B **35**, 2130006 (2021).
- [57] R. G. Pereira and R. Egger, *Electrical Access to Ising Anyons in Kitaev Spin Liquids*, Phys. Rev. Lett. **125**, 227202 (2020).
- [58] J. Aftergood and S. Takei, *Probing quantum spin liquids in equilibrium using the inverse spin Hall effect*, Phys. Rev. Research **2**, 033439 (2020).

- [59] T. Minakawa, Y. Murakami, A. Koga, and J. Nasu, *Majorana-Mediated Spin Transport in Kitaev Quantum Spin Liquids*, Phys. Rev. Lett. **125**, 047204 (2020).
- [60] E. J. König, M. T. Randeria, and B. Jäck, *Tunneling Spectroscopy of Quantum Spin Liquids*, Phys. Rev. Lett. **125**, 267206 (2020).

SUPPLEMENTAL MATERIAL

Suppression of Antiferromagnetic Order by Strain in Honeycomb Cobaltate: Implication for Quantum Spin Liquid

Gye-Hyeon Kim,^{1*} Miju Park,^{1*} Uksam Choi,¹ Baekjune Kang,¹ Uihyeon Seo,¹ GwangCheol Ji,²
Seunghyeon Noh,³ Deok-Yong Cho,⁴ Jung-Woo Yoo,³ Jong Mok Ok,² and Changhee Sohn^{1†}

*¹Department of Physics, Ulsan National Institute of Science and Technology,
Ulsan, 44919, Republic of Korea.*

²Department of Physics, Pusan National University, Pusan, 46241, Republic of Korea.

*³Department of Materials Science and Engineering, Ulsan National Institute of Science and Technology,
Ulsan, 44919, Republic of Korea.*

⁴Department of Physics, Jeonbuk National University, Jeonju, 54896, Republic of Korea.

Contents

1. Layered structure of Co-based d^7 honeycomb oxides $A_3Co_2SbO_6$ ($A = Na, \text{ and } Cu$)
2. Effect of Sb^{5+} and O^{2-} crystal field in Co^{2+} orbitals
3. X-ray absorption spectroscopy measurements setup
4. Peak assignment in O K -edge X-ray absorption spectra for $Na_3Co_2SbO_6$ and $Cu_3Co_2SbO_6$
5. Detailed structure analyses of ultrathin and helium implanted $Cu_3Co_2SbO_6$ films
6. Crystal field multiplet simulation for Co L_3 -edge X-ray linear dichroism
7. Optical spectra, excitonic transition, and spin-exciton coupling in $Cu_3Co_2SbO_6$ films
8. Magnetic susceptibility of $Na_3Co_2SbO_6$ and $Cu_3Co_2SbO_6$ thin films
9. Reversal effect of helium ion implantation in crystal structure and T_N of $Cu_3Co_2SbO_6$
10. SRIM/TRIM Monte Carlo simulation for helium ion implantation
11. Full data of X-ray absorption spectroscopy measurements

1. Layered structure of Co-based d^7 honeycomb oxides $A_3Co_2SbO_6$ ($A= Na, \text{ and } Cu$)

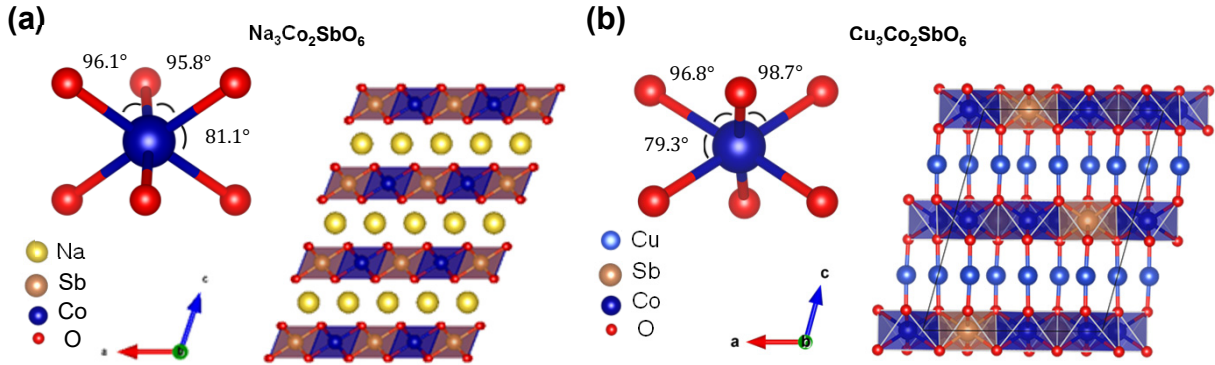


FIG. S1. The Co-based d^7 layered honeycomb oxides, (a) $Na_3Co_2SbO_6$ ($C 2/m$ space group) and (b) $Cu_3Co_2SbO_6$ ($C 2/c$ space group). In both cases, a Co-Sb layer and an A-site cation layer (Na^+ and Cu^+ , respectively) are stacked similarly to the well-known delafossite-type structure. The Co-Sb layer has CoO_6 octahedra with compressive trigonal distortion.

2. Effect of Sb^{5+} and O^{2-} crystal field in Co^{2+} orbitals

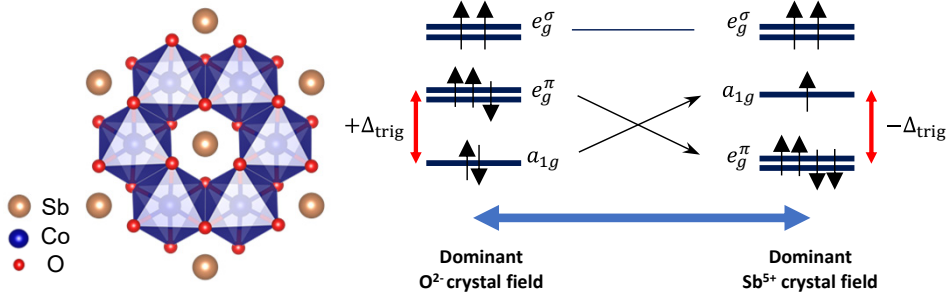


FIG. S2. Top view of layered honeycomb cobaltates with triangular Sb^{5+} lattice (left) and orbital structures of Co^{2+} ion with respect to trigonal crystal field Δ_{trig} (right). The orbital structures of Co^{2+} ions are influenced by both Sb^{5+} and O^{2-} crystal field. Note that, the sign of the field from Sb^{5+} ions is opposite to that from O^{2-} ions due to its positive charge. Therefore, the sign of the total Δ_{trig} is determined by whether the crystal field from Sb^{5+} or O^{2-} ions is dominant.

3. X-ray absorption spectroscopy measurements setup

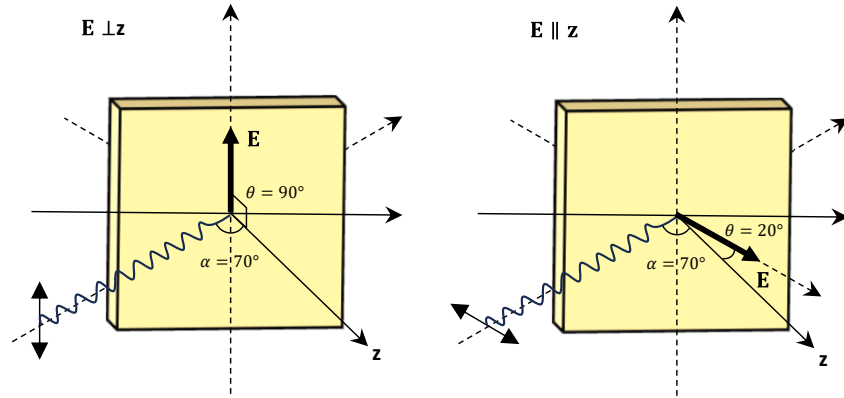


FIG. S3. Experimental geometry of X-ray absorption spectroscopy with surface horizontally polarized (*p*-polarized, left) and surface vertically polarized (*s*-polarized, right) incident beam. The θ is defined as the angle between the electric field vector \mathbf{E} and the out-of-plane direction of the samples. The angle α , the angle between the out-of-plane direction of samples and the incident angle of the X-ray beam, has set to 70° .

4. Peak assignment in O K -edge X-ray absorption spectra for $\text{Na}_3\text{Co}_2\text{SbO}_6$ and $\text{Cu}_3\text{Co}_2\text{SbO}_6$

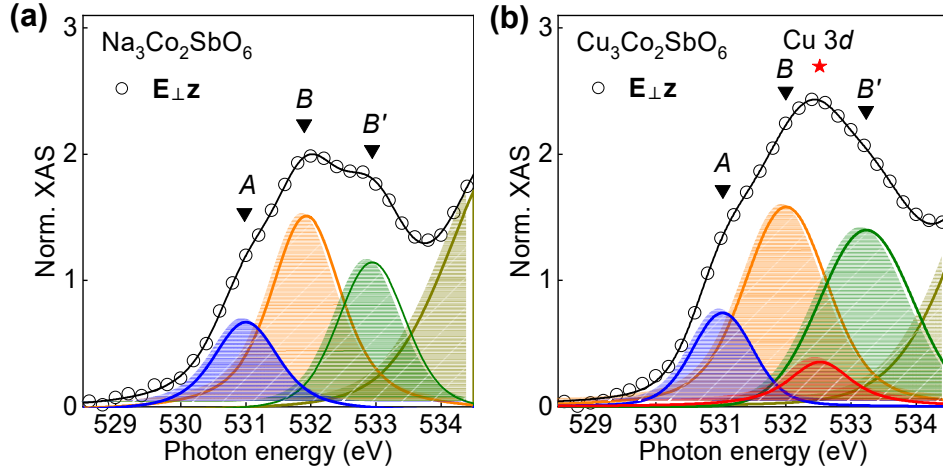


FIG. S4. (a) $I_{\perp z}$ of O K -edge X-ray absorption spectroscopy in $\text{Na}_3\text{Co}_2\text{SbO}_6$. Three peaks labeled A , B , and B' are associated with the Co $3d$ orbitals. Peak A is assigned as the electron transition from O $1s$ to O $2p$ orbitals hybridized Co t_{2g} orbitals (final state of 3A_2) [44]. Both peak B and B' are from O $2p$ orbitals hybridized Co e_g^σ orbitals with final states of 3T_2 and 3T_1 , respectively [44]. (b) $I_{\perp z}$ of O K -edge X-ray absorption spectroscopy in $\text{Cu}_3\text{Co}_2\text{SbO}_6$. Similar peak features of A , B , and B' are also shown at almost identical photon energy. Note that Cu $3d$ peak at 532.5 eV is related to the O $2p$ states hybridized with Cu $3d$ orbitals in Cu^+ ions [45,46].

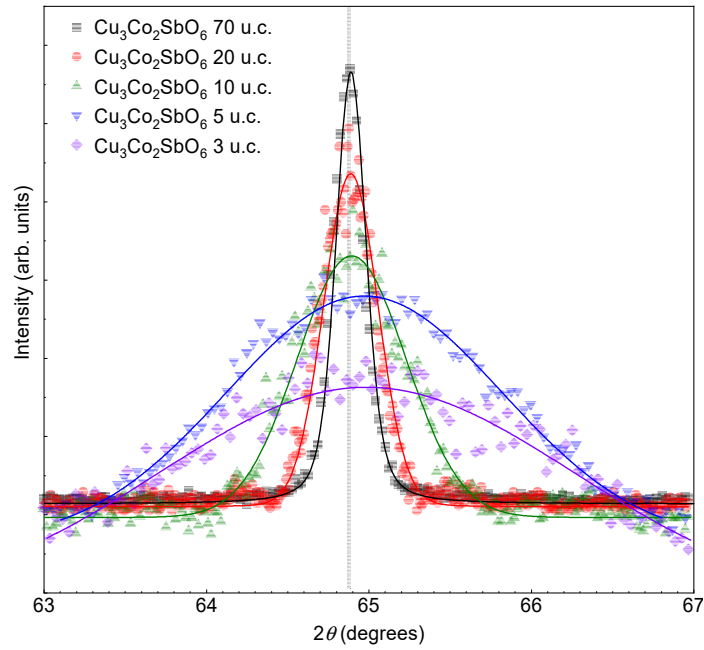


FIG. S5. θ - 2θ (00 l) scan of ZnO (008) plane for thickness-dependent $\text{Cu}_3\text{Co}_2\text{SbO}_6$ thin films (dot line) with fitting results (solid line) in linear scale. The peak position for bulk-like 70 unit-cell (u.c.) thick $\text{Cu}_3\text{Co}_2\text{SbO}_6$ thin film is marked as a grey solid line. The (008) peak of $\text{Cu}_3\text{Co}_2\text{SbO}_6$ films are gradually shifted to a higher angle from 70 u.c. to 3 u.c. due to the tensile strain from ZnO substrate. This shift indicates the contraction in the out-of-plane lattice constant c^* of thickness-controlled $\text{Cu}_3\text{Co}_2\text{SbO}_6$.

5. Detailed structure analyses of ultrathin and helium implanted $\text{Cu}_3\text{Co}_2\text{SbO}_6$ films

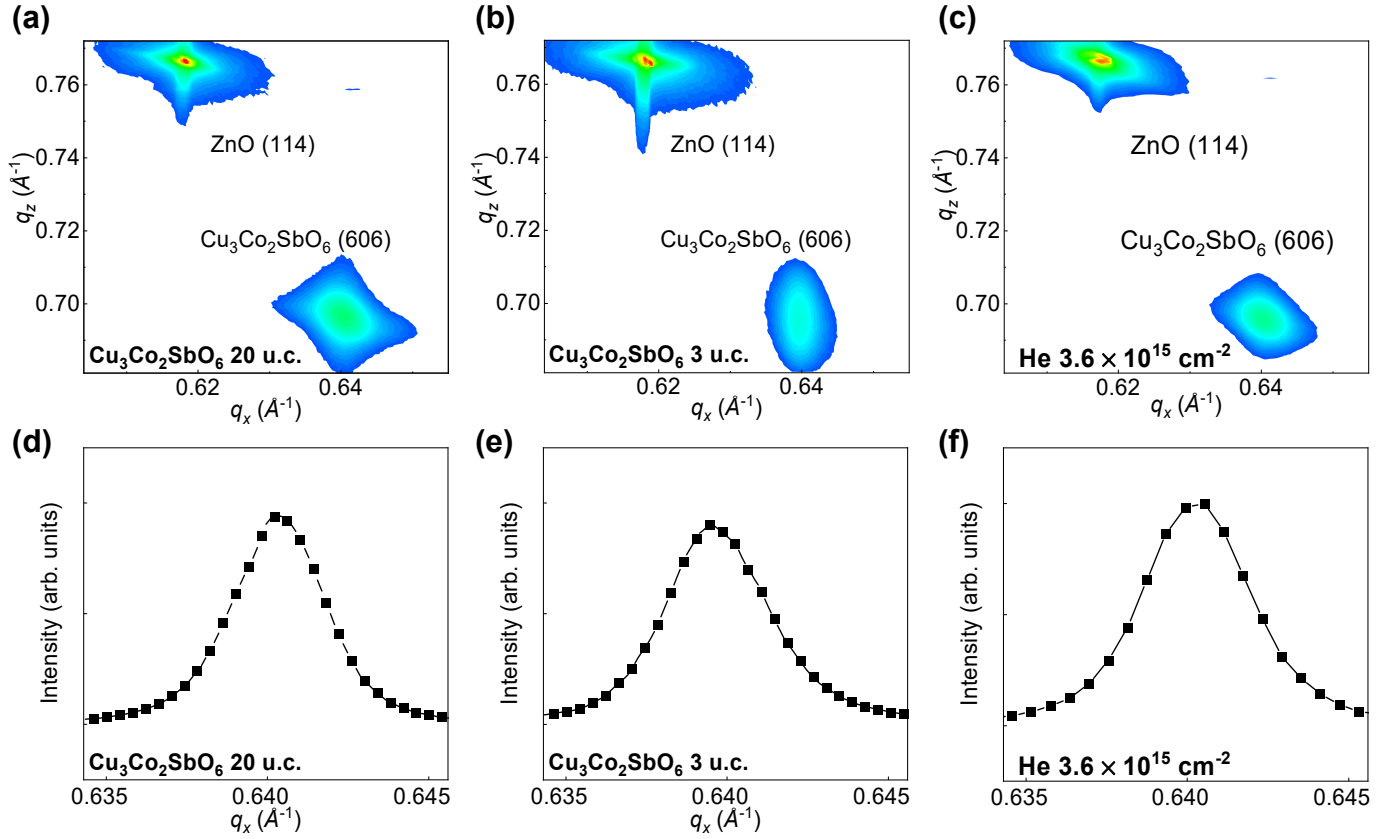


FIG. S6. Reciprocal space mapping of ZnO (114) plane for (a) bulk-like 20 unit-cell (u.c.), (b) ultrathin 3 u.c., and (c) $\text{He } 3.6 \times 10^{15} \text{ cm}^{-2}$ $\text{Cu}_3\text{Co}_2\text{SbO}_6$ thin films. The (606) peak of $\text{Cu}_3\text{Co}_2\text{SbO}_6$ is shown in all thin films. The q_x profiles of (d) bulk-like 20 u.c., (e) ultrathin 3 u.c., and (f) $\text{He } 3.6 \times 10^{15} \text{ cm}^{-2}$ $\text{Cu}_3\text{Co}_2\text{SbO}_6$ thin films are extracted from the reciprocal space mapping data.

6. Crystal field multiplet simulation for Co L_3 -edge X-ray linear dichroism

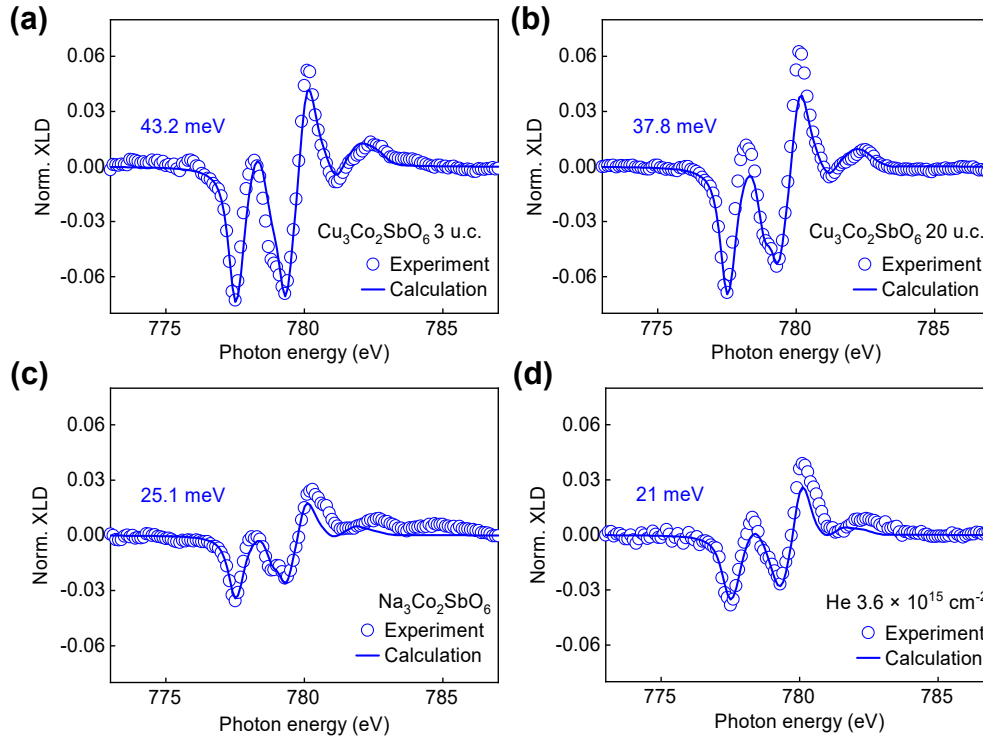


FIG. S7. Experimental X-ray linear dichroism data (open circle) and the simulation from crystal field multiplet calculation (solid line) of (a) 3 unit-cell (u.c.) $\text{Cu}_3\text{Co}_2\text{SbO}_6$ film, (b) 20 u.c. $\text{Cu}_3\text{Co}_2\text{SbO}_6$ film, (c) $\text{Na}_3\text{Co}_2\text{SbO}_6$ film, and (d) He $3.6 \times 10^{15} \text{ cm}^{-2}$ implanted $\text{Cu}_3\text{Co}_2\text{SbO}_6$ film. Within the trigonal symmetry calculation, the magnitude of the trigonal crystal field Δ_{trig} is deduced to be 43.2 meV for 3 u.c. $\text{Cu}_3\text{Co}_2\text{SbO}_6$ film, 37.8 meV for 20 u.c. $\text{Cu}_3\text{Co}_2\text{SbO}_6$, 25.1 meV for $\text{Na}_3\text{Co}_2\text{SbO}_6$, and 21 meV for He $3.6 \times 10^{15} \text{ cm}^{-2}$ implanted $\text{Cu}_3\text{Co}_2\text{SbO}_6$ film.

7. Optical spectra, excitonic transition, and spin-exciton coupling in $\text{Cu}_3\text{Co}_2\text{SbO}_6$ films

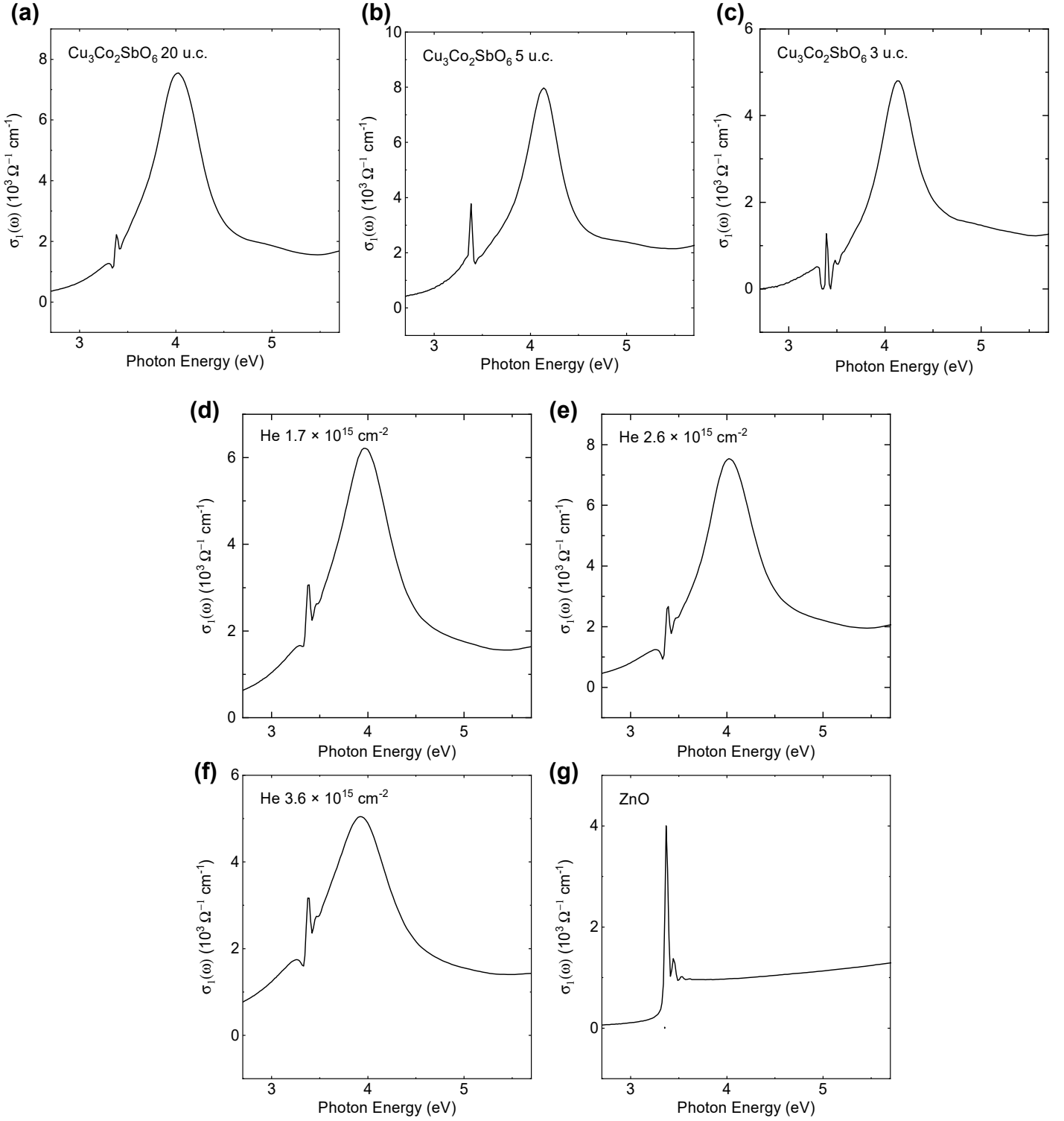


FIG. S8. Optical conductivity $\sigma_1(\omega)$ at 7 K of (a) 20 unit-cell (u.c.) $\text{Cu}_3\text{Co}_2\text{SbO}_6$ film, (b) 5 u.c. $\text{Cu}_3\text{Co}_2\text{SbO}_6$ film, (c) 3 u.c. $\text{Cu}_3\text{Co}_2\text{SbO}_6$ film, (d) $1.7 \times 10^{15} \text{cm}^{-2}$ implanted $\text{Cu}_3\text{Co}_2\text{SbO}_6$ film, (e) $2.6 \times 10^{15} \text{cm}^{-2}$ implanted $\text{Cu}_3\text{Co}_2\text{SbO}_6$ film, (f) $3.6 \times 10^{15} \text{cm}^{-2}$ implanted $\text{Cu}_3\text{Co}_2\text{SbO}_6$ film and (g) ZnO substrate. All the strong excitonic excitation, attributed to the $\text{Cu } 3d \rightarrow \text{Co } 3d e_g$ transition, are located near 4 eV. A sharp anomaly near 3.35 eV in optical spectra of $\text{Cu}_3\text{Co}_2\text{SbO}_6$ films is an artifact from sharp excitations in ZnO substrates.

8. Magnetic susceptibility of $\text{Na}_3\text{Co}_2\text{SbO}_6$ and $\text{Cu}_3\text{Co}_2\text{SbO}_6$ thin films

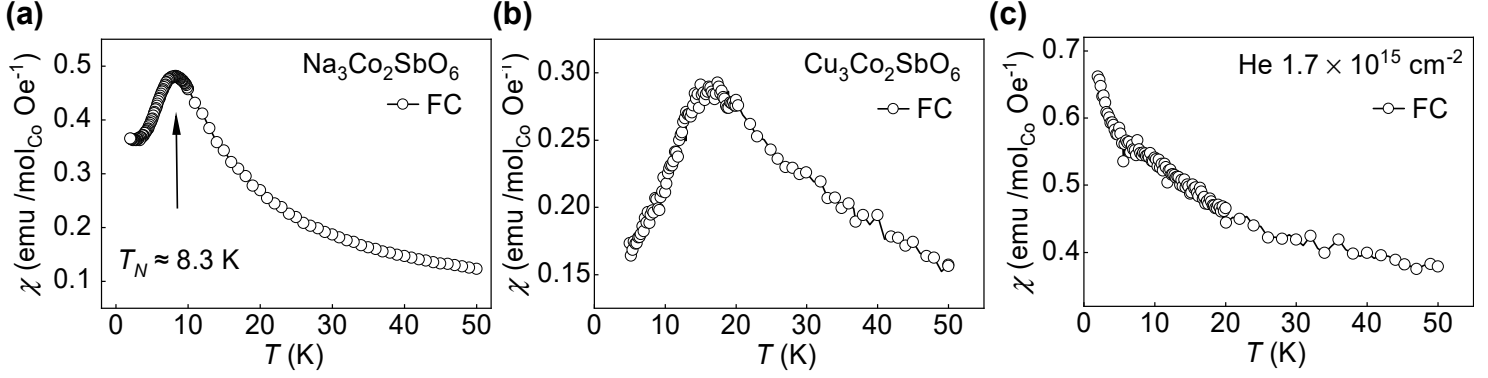


FIG. S9. Magnetic susceptibility $\chi(T)$ of (a) $\text{Na}_3\text{Co}_2\text{SbO}_6$ film, (b) pristine $\text{Cu}_3\text{Co}_2\text{SbO}_6$ film, and (c) He $1.7 \times 10^{15} \text{ cm}^{-2}$ implanted $\text{Cu}_3\text{Co}_2\text{SbO}_6$ film. All data are estimated from 0.1 T Field-cooled magnetization curves. For $\text{Na}_3\text{Co}_2\text{SbO}_6$ film and pristine $\text{Cu}_3\text{Co}_2\text{SbO}_6$ film, clear antiferromagnetic transitions are shown at about 8 K, and 16 K, respectively. It is consistent with previous studies on the bulk $\text{Na}_3\text{Co}_2\text{SbO}_6$ [44] and $\text{Cu}_3\text{Co}_2\text{SbO}_6$ [31]. However, helium implanted $\text{Cu}_3\text{Co}_2\text{SbO}_6$ exhibits additional paramagnetic signal at low T , indicating formation of paramagnetic impurity during helium ion implantation. It significantly hinders the precise determination of T_N in helium implanted $\text{Cu}_3\text{Co}_2\text{SbO}_6$ by using conventional susceptibility measurement.

9. Reversal effect of helium ion implantation in crystal structure and T_N of $\text{Cu}_3\text{Co}_2\text{SbO}_6$

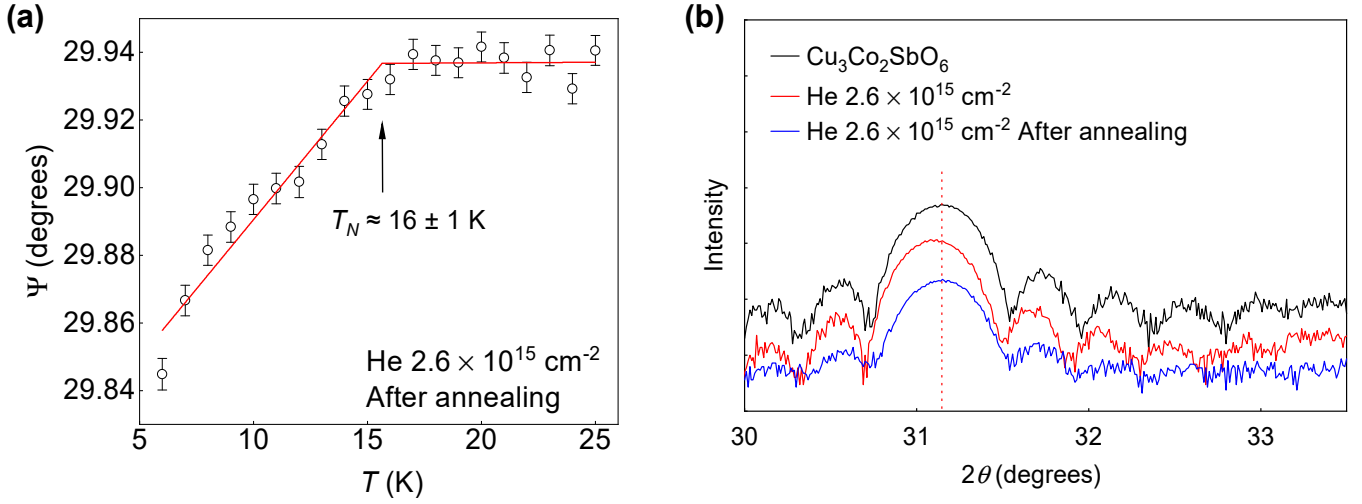


FIG. S10. (a) T -dependent ellipsometry parameter Ψ , where $\tan\Psi$ correspond to amplitude ratio between reflected p - and s -polarized light, and (b) X-ray diffraction of helium implanted $\text{Cu}_3\text{Co}_2\text{SbO}_6$ thin film before and after thermal annealing to remove helium ions. Helium implanted $\text{Cu}_3\text{Co}_2\text{SbO}_6$ film was annealed at 250 °C, 3 hours in ambient pressure. Both data show reversible effect of helium ion implantation via post-annealing. In (a), the T_N of 9.3 K before the annealing [Fig. 5(e) in the main manuscript] is returned to 16 K like in pristine $\text{Cu}_3\text{Co}_2\text{SbO}_6$ film. In (b), the shifted (004) peak of the helium implanted $\text{Cu}_3\text{Co}_2\text{SbO}_6$ is recovered to the original position of pristine $\text{Cu}_3\text{Co}_2\text{SbO}_6$ film. Furthermore, the retained thickness fringes demonstrate the high quality of the film, with no indications of damage resulting from the implantation and removal of helium ions.

10. SRIM/TRIM Monte Carlo simulation for helium ion implantation

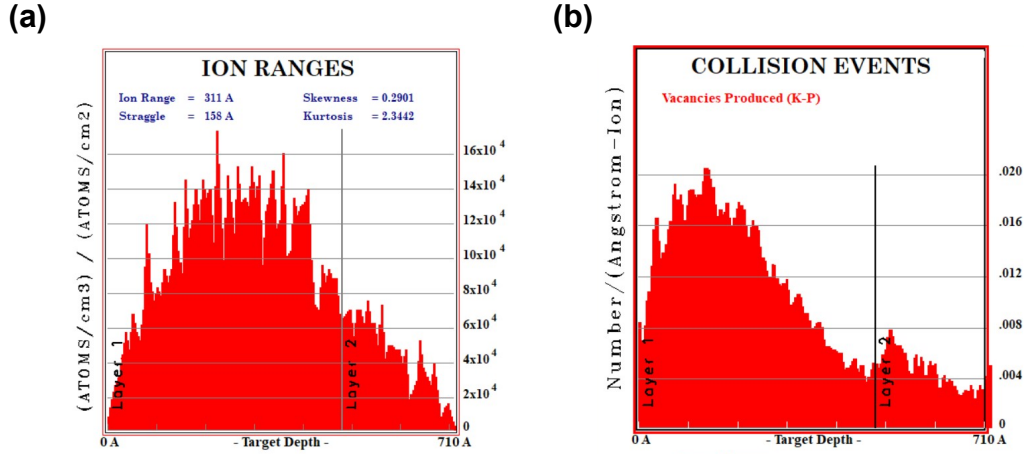


FIG. S11. Stopping and Range of Ions in Matter / Transport of Ions in Matter (SRIM/TRIM) Monte Carlo Simulation for helium ion implantation. (a) The spatial distribution of helium ions within a thin film composed of $\text{Cu}_3\text{Co}_2\text{SbO}_6$, with a gold layer deposited on top, when helium ions with energy of 10 keV are incident upon it. (b) The generation of vacancies resulting from helium ions collisions within the gold coated $\text{Cu}_3\text{Co}_2\text{SbO}_6$ thin film. Layer 1 is the gold layer with a thickness of 48 nm, while Layer 2 is the $\text{Cu}_3\text{Co}_2\text{SbO}_6$ layer with a thickness of 23 nm. It is noteworthy that we carefully determined the thickness of the gold layer through simulations to ensure that helium ions incident upon the $\text{Cu}_3\text{Co}_2\text{SbO}_6$ thin film do not cause substantial damage [34]. Given the linear distribution of helium ions within the $\text{Cu}_3\text{Co}_2\text{SbO}_6$ thin film, we computed the density of helium ions per unit volume in Layer 2 as half of the density value at the interface between gold and $\text{Cu}_3\text{Co}_2\text{SbO}_6$ thin film, multiplied by the incident fluence.

11. Full data of X-ray absorption spectroscopy measurements

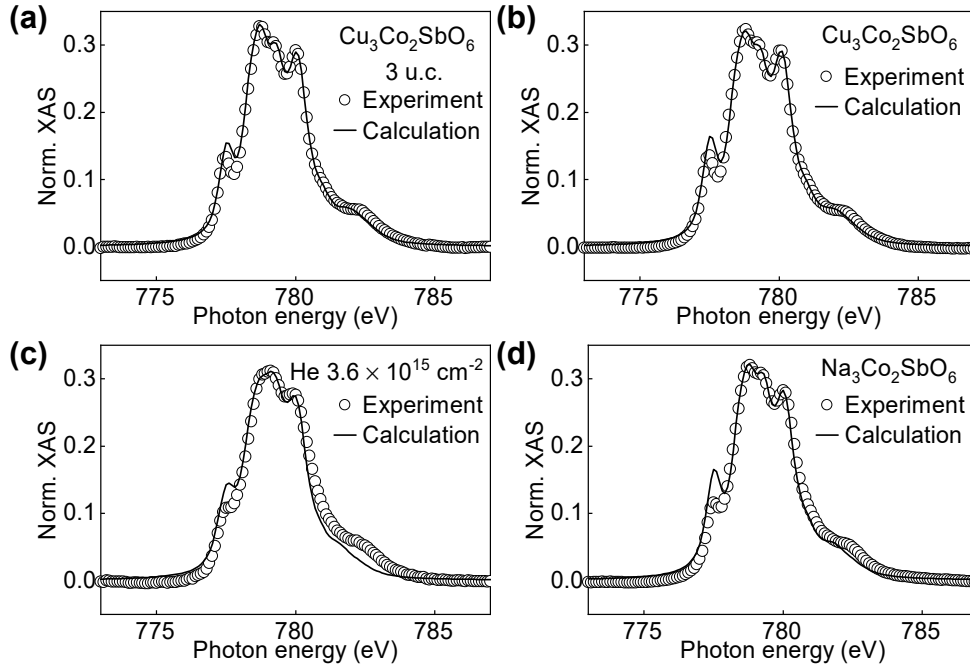


FIG. S12. Experimental and simulated isotropic Co L_3 -edge spectra of (a) 3 unit-cell $\text{Cu}_3\text{Co}_2\text{SbO}_6$ film, (b) $\text{Cu}_3\text{Co}_2\text{SbO}_6$ film, (c) $\text{He } 3.6 \times 10^{15} \text{ cm}^{-2}$ implanted $\text{Cu}_3\text{Co}_2\text{SbO}_6$ film, and (d) $\text{Na}_3\text{Co}_2\text{SbO}_6$ films.

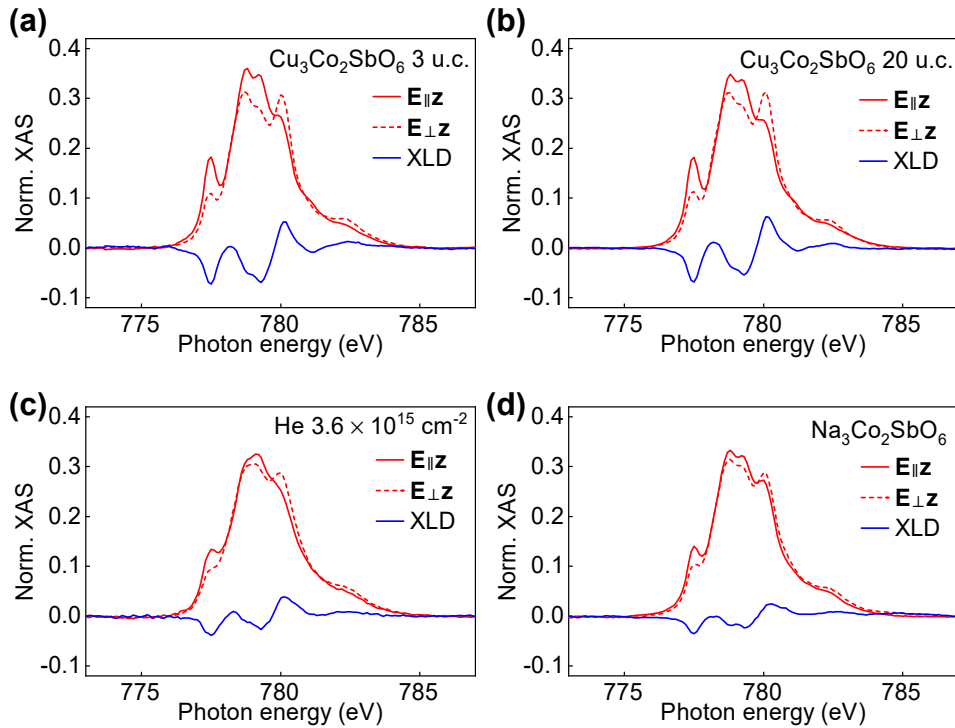


FIG. S13. The normalized polarized spectra and X-ray linear dichroism of (a) 3 unit-cell $\text{Cu}_3\text{Co}_2\text{SbO}_6$ film, (b) pristine 20 unit-cell $\text{Cu}_3\text{Co}_2\text{SbO}_6$ film, (c) $\text{He } 3.6 \times 10^{15} \text{ cm}^{-2}$ implanted $\text{Cu}_3\text{Co}_2\text{SbO}_6$ film, and (d) $\text{Na}_3\text{Co}_2\text{SbO}_6$ film.

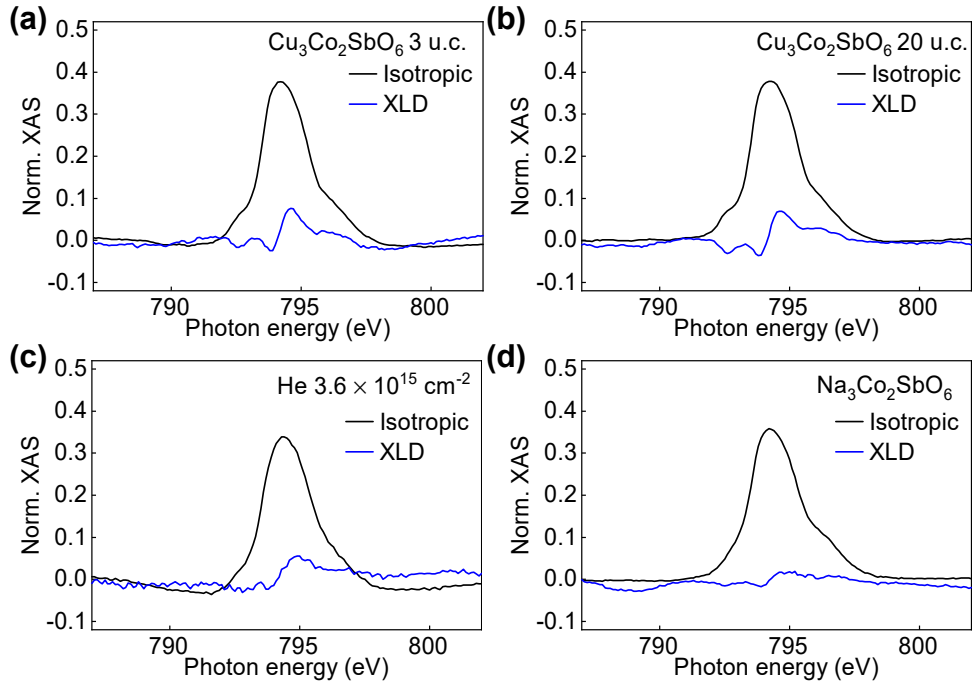


FIG. S14. The normalized Co L_2 -edge isotropic and XLD spectra of (a) 3 unit-cell $\text{Cu}_3\text{Co}_2\text{SbO}_6$ film, (b) pristine 20 unit-cell $\text{Cu}_3\text{Co}_2\text{SbO}_6$ film, (c) He $3.6 \times 10^{15} \text{ cm}^{-2}$ implanted $\text{Cu}_3\text{Co}_2\text{SbO}_6$ film, and (d) $\text{Na}_3\text{Co}_2\text{SbO}_6$ film. The Co L_2 -edge spectra exhibit a similar trend to the Co L_3 -edge spectra.

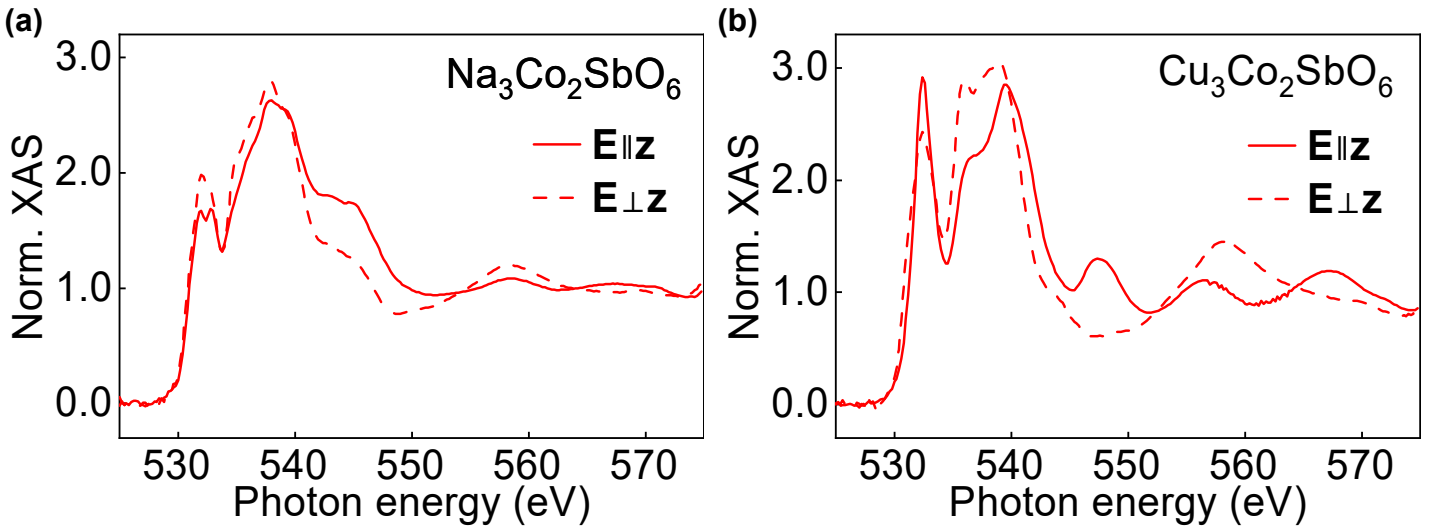


FIG. S15. The normalized O K -edge spectra of (a) $\text{Na}_3\text{Co}_2\text{SbO}_6$ film and (b) $\text{Cu}_3\text{Co}_2\text{SbO}_6$ film from 525 eV to 575 eV. It could be assumed the complicated hybridization due to the unoccupied state of the O $2p$ orbital is in high energy [42]. These O K -edge spectra were normalized at 545 eV–575 eV.